

Photoacoustic Microscopy and Computed Tomography: From Bench to Bedside

Lihong V. Wang* and Liang Gao*

Optical Imaging Laboratory, Department of Biomedical Engineering, Washington University in St. Louis, St. Louis, Missouri 63130; email: lhwang@wustl.edu

Annu. Rev. Biomed. Eng. 2014. 16:155–85

First published online as a Review in Advance on May 28, 2014

The *Annual Review of Biomedical Engineering* is online at bioeng.annualreviews.org

This article's doi:
10.1146/annurev-bioeng-071813-104553

Copyright © 2014 by Annual Reviews.
All rights reserved

*Equal contribution

Keywords

biomedical imaging, label-free imaging, small-animal imaging, cancer diagnosis, human imaging

Abstract

Photoacoustic imaging (PAI) of biological tissue has seen immense growth in the past decade, providing unprecedented spatial resolution and functional information at depths in the optical diffusive regime. PAI uniquely combines the advantages of optical excitation and those of acoustic detection. The hybrid imaging modality features high sensitivity to optical absorption and wide scalability of spatial resolution with the desired imaging depth. Here we first summarize the fundamental principles underpinning the technology, then highlight its practical implementation, and finally discuss recent advances toward clinical translation.

Contents

1. INTRODUCTION	156
2. PRINCIPLES	157
2.1. Time-Domain Photoacoustics	157
2.2. Frequency-Domain Photoacoustics	159
2.3. Signal-to-Noise Ratios in the Time and Frequency Domains	160
3. MULTISCALE PHOTOACOUSTIC TOMOGRAPHY AND MAJOR IMPLEMENTATIONS	161
3.1. Optical-Resolution Photoacoustic Microscopy	161
3.2. Acoustic-Resolution Photoacoustic Microscopy	164
3.3. Photoacoustic Computed Tomography	164
3.4. Photoacoustic Endoscopy	165
3.5. Optical-Detection Photoacoustic Tomography	165
4. QUANTITATIVE PHOTOACOUSTIC SENSING AND IMAGING	169
4.1. Photoacoustic Oximetry	169
4.2. Photoacoustic Thermometry	170
4.3. In Vivo Photoacoustic Flowmetry	171
4.4. In Vivo Photoacoustic Flow Cytometry	173
4.5. Förster Resonance Energy Transfer Photoacoustic Microscopy	174
4.6. Stimulated Raman Photoacoustic Microscopy	174
5. TECHNICAL ADVANCES FROM BENCH TO BEDSIDE	176
5.1. Breast Cancer Imaging	176
5.2. Brain Imaging	176
5.3. Sentinel Lymph Node Mapping	178
5.4. Current Progress Toward Clinical Use	178
6. CONCLUSIONS AND OUTLOOK	179

1. INTRODUCTION

The photoacoustic (PA) effect refers to the phenomenon of generating acoustic waves from an object being illuminated by pulsed or intensity-modulated, continuous-wave (CW) electromagnetic waves, especially light. Although its first demonstration by Alexander Graham Bell dates back to 1880 (1), the PA effect has been widely exploited only recently in a number of fields, ranging from basic sciences to engineering (2, 3). In biomedicine, the application of the PA effect started in the 1970s (4); however, it was not until the last decade of the twentieth century that breakthroughs were achieved in demonstrating the PA effect in optically scattering media and biological tissue (5, 6). In particular, the demonstration of functional PA imaging (PAI) propelled the field into fast development (7). PAI has now become one of the largest research areas in the field of biomedical optics.

PAI combines the advantages of both optical excitation and acoustic detection, resulting in a hybrid imaging modality that has high sensitivity to optical absorption (8) and the capability for deep imaging in soft tissue. Although pure optical-imaging methods can also detect optical absorption by measuring the intensity variation in transmitted or reflected light, they are generally two orders of magnitude less sensitive than PAI (9). Additionally, because an acoustic wave has a much lower scattering coefficient in biological tissue than light does, PAI offers high-spatial-resolution

PAI: photoacoustic imaging

imaging at greater depths than conventional optical-imaging methods do, thereby breaking through the optical diffusion limit ultrasonically.

Cross-sectional or three-dimensional (3D) PAI is referred to as photoacoustic tomography (PAT). The spatial resolution and imaging depth within the reach of diffusive photons in PAT are highly scalable. In the diffusive regime, the spatial resolution of PAT is derived from ultrasonic detection. As the ultrasonic center frequency and bandwidth increase, the spatial resolution improves at the expense of a decreased imaging depth because higher-frequency ultrasound experiences more attenuation, and vice versa. The depth-to-resolution ratio is determined by the space-bandwidth product a modality can measure in volumetric imaging. In PAT, the depth-to-resolution ratio is ~ 200 (10), nearly two orders of magnitude higher than that in diffuse optical tomography (11).

In this review, we introduce the fundamental principles of PAI in the time and frequency domains and theoretically compare their signal-to-noise ratios (SNRs) based on laser safety standards. Then we discuss multiscale PAT and its major implementation and the role of PAT in quantitative measurements. After that, current technical advances toward translational PAT are reviewed. Finally, we summarize the field and explore future directions.

PAT: photoacoustic tomography

2. PRINCIPLES

Upon absorbing a photon, a molecule transitions from the ground state to an excited state. Energy is released primarily via two paths: radiative decay (i.e., fluorescence) and nonradiative decay (thermal dissipation). If the excitation light is a short pulse (time domain) or is intensity modulated (frequency domain), the generated heat during nonradiative decay produces, via thermoelastic expansion, an ultrasonic wave, which is referred to as the PA wave. The fundamental principles of PAI in the time and frequency domains are addressed in this section.

2.1. Time-Domain Photoacoustics

There are two important timescales associated with pulsed laser heating: thermal relaxation time and stress relaxation time. The excitation is defined as being thermally or stress confined if the laser pulse duration is much shorter than the corresponding relaxation time (see Sidebar, Thermal and Stress Relaxation Times).

Upon excitation, the fractional volume expansion dV/V can be expressed as

$$\frac{dV}{V} = -\kappa p + \beta T. \quad (1)$$

Here κ is the isothermal compressibility (Pa^{-1}), and β is the thermal coefficient of volume expansion (K^{-1}). p and T denote the pressure (Pa) and temperature (K), respectively. Provided that the thermal and stress confinements are both satisfied, the fractional volume expansion is negligible, and the pressure immediately builds up within the heated region. The initial pressure rise p_0 can

THERMAL AND STRESS RELAXATION TIMES

The thermal relaxation time characterizes the thermal diffusion over a region and is estimated by $\tau_{\text{th}} = d_c^2/\alpha_{\text{th}}$, where α_{th} is the thermal diffusivity (m^2/s), and d_c is the characteristic dimension of the heated region or the desired spatial resolution. The stress relaxation time describes the pressure propagation and is given by $\tau_s = d_c/v_s$, where v_s is the speed of sound (m/s).

be derived from Equation 1:

$$p_0 = \frac{\beta T}{\kappa}, \quad (2)$$

which can be rewritten as

$$p_0 = \frac{\beta}{\kappa} \frac{\eta_{\text{th}} A_e}{\rho C_V}. \quad (3)$$

Here A_e is the specific optical absorption (J/m^3), η_{th} is the percentage of absorbed energy that is converted to heat, ρ is the mass density (kg/m^3), and C_V is the specific heat capacity at constant volume [$\text{J}/(\text{kg}\cdot\text{K})$]. To simplify Equation 3, a dimensionless quantity, the Grüneisen parameter, is defined as

$$\Gamma = \frac{\beta}{\kappa \rho C_V}. \quad (4)$$

Substituting Γ into Equation 3 yields

$$p_0 = \Gamma \eta_{\text{th}} A_e. \quad (5)$$

For linear optical absorption—that is, when A_e is proportional to the local optical fluence F (J/cm^2)—Equation 5 becomes

$$p_0 = \Gamma \eta_{\text{th}} \mu_a F, \quad (6)$$

where μ_a is the optical absorption coefficient (cm^{-1}).

The rapid deposition of laser energy causes an immediate increase in pressure within the heated region. Under conditions of thermal linearity (12) and thermal confinement, the release of this pressure through thermoelastic expansion gives rise to an ultrasonic wave. The acoustic pressure p of the ultrasonic wave is governed by the following wave equation (13):

$$\left(\nabla^2 - \frac{1}{v_s^2} \frac{\partial^2}{\partial t^2} \right) p = -\frac{\beta}{C_p} \frac{\partial H}{\partial t}. \quad (7)$$

Here C_p is the specific heat capacity at constant pressure [$\text{J}/(\text{kg}\cdot\text{K})$]. H is the heating function defined as the heat deposited per unit volume and per unit time, and H is related to the specific optical absorption A_e by $H = \eta_{\text{th}} \frac{\partial A_e}{\partial t}$.

The spatial and temporal profiles of pressure $p(\vec{r}, t)$ derived from Equation 7 are affected by the geometry of an absorber (14), the laser pulse duration (14), the mass density ratio $\hat{\rho}$ and sound speed ratio \hat{v}_s of the absorber to surrounding media (13), and the ultrasonic attenuation (15). Under conditions of delta-pulse excitation, $\hat{\rho} = 1$, $\hat{v}_s = 1$, and zero ultrasonic attenuation loss, a forward solution to Equation 7 is

$$p_{\delta T}(\vec{r}, t) = \frac{1}{4\pi v_s^2} \frac{\partial}{\partial t} \left[\int d\vec{r}' \frac{p_0(\vec{r}')}{|\vec{r} - \vec{r}'|} \delta \left(t - \frac{|\vec{r} - \vec{r}'|}{v_s} \right) \right], \quad (8)$$

where $p_0(\vec{r}')$ is the initial pressure rise at position \vec{r}' (16). If the pulsed excitation has a finite duration, the pressure waveform can be computed by a convolution with the delta-pulse response:

$$p(\vec{r}, t) = \int_{-\infty}^{\infty} dt' p_{\delta T}(\vec{r}, t - t') H(t'), \quad (9)$$

where $H(t)$ is the temporal profile of the excitation pulse. For monopole radiation—that is, radiation from a point absorber at $\vec{r}' = 0$ (12)—Equation 8 becomes

$$p_{\delta T, \delta D}(\vec{r}, t) = \frac{1}{4\pi v_s^2} \frac{p_0}{|\vec{r}|} \frac{d}{dt} \left[\delta \left(t - \frac{|\vec{r}|}{v_s} \right) \right]. \quad (10)$$

Substituting Equation 10 into Equation 9 yields

$$p_{\delta D}(\vec{r}, t) = \frac{1}{4\pi v_s^2} \frac{p_0}{|\vec{r}|} \frac{d}{dt} H\left(t - \frac{|\vec{r}|}{v_s}\right). \quad (11)$$

Equation 11 implies that, in time-domain PAI, the monopole PA amplitude is proportional to the product of the initial pressure rise p_0 at the origin and the first time derivative of the excitation pulse temporal profile $H(t)$.

Equations 8–11 are based on the hypothesis that there is no ultrasonic loss during propagation; however, because most time-domain PAI methods collect broadband ultrasonic signals, the frequency-dependent ultrasonic attenuation becomes a dominating factor when one calculates the pressure in the far field (15). Consequently, the pressure waveform $p(\vec{r}, t)$ is subject to filtering with the ultrasonic attenuation function $U(\omega)$ of the medium:

$$p^*(\vec{r}, t) = \mathbb{F}^{-1}[\mathbb{F}(p(\vec{r}, t))U(\omega)], \quad (12)$$

where \mathbb{F} denotes Fourier transformation. For water and muscle, $U(\omega)$ has a form of $\exp(-\alpha \frac{\omega^2}{4\pi^2} r)$ and $\exp(-\alpha \frac{\omega}{2\pi} r)$, respectively (17), where α denotes the ultrasonic attenuation coefficient (Hz^{-2}/m or Hz^{-1}/m). Equation 12 implies that the ultrasonic attenuation not only reduces the PA amplitude but also broadens the PA wave temporal profile, thereby degrading the spatial resolution in acquired images (15). To improve image quality, the ultrasonic attenuation can be accounted for mathematically (18, 19).

2.2. Frequency-Domain Photoacoustics

The analytical description of frequency-domain PAI is most conveniently formulated by utilizing the Fourier transformation. Below, a tilde above a variable denotes the Fourier transform of the variable. Equation 7 is Fourier transformed into an inhomogeneous Helmholtz equation:

$$(\nabla^2 + k^2)\tilde{p}(\vec{r}, \omega) = -\frac{i\omega\beta}{C_p} \tilde{H}(\vec{r}, \omega), \quad (13)$$

where $k = \omega/v_s$ is the acoustic wave number. Note that heat diffusion is ignored even when the sinusoidal excitation lasts longer than the thermal relaxation time. A general Green's function solution of Equation 13 for unbounded media is

$$\tilde{p}(\vec{r}, \omega) = -\frac{i\omega\beta}{4\pi C_p} \int \frac{e^{ik|\vec{r}-\vec{r}'|}}{|\vec{r}-\vec{r}'|} \tilde{H}(\vec{r}', \omega) d\vec{r}'. \quad (14)$$

Equation 14 implies that, in frequency-domain PAI, the PA amplitude is proportional to the modulation frequency ω at the origin.

In the far field, where $|\vec{r}| \gg |\vec{r}'|$, we have $|\vec{r}-\vec{r}'| \approx |\vec{r}| - \hat{r} \cdot \vec{r}'$, and Equation 14 becomes

$$\tilde{p}(\vec{r} \gg \vec{r}', \omega) = -\frac{i\omega\beta}{4\pi C_p} \frac{e^{ik|\vec{r}|}}{|\vec{r}|} \int e^{-ik\hat{r} \cdot \vec{r}'} \tilde{H}(\vec{r}', \omega) d\vec{r}'. \quad (15)$$

For monopole radiation, we have $\tilde{H}(\vec{r}', \omega) = \mu_a \bar{I} \eta_{\text{th}} \delta(\vec{r}')$, where \bar{I} is the average laser fluence rate. Accordingly, Equation 15 becomes

$$\tilde{p}_{\delta D}(\vec{r}, \omega) = -\frac{i\omega\beta\mu_a \bar{I} \eta_{\text{th}}}{4\pi C_p} \frac{e^{ik|\vec{r}|}}{|\vec{r}|}. \quad (16)$$

The harmonic PA signal (Equation 16) can be measured with a high SNR by lock-in detection (20). However, it is not suitable for depth-resolved imaging owing to phase wrapping at a single frequency. In order to achieve sectioning capability, chirped optical excitation has been exploited (21–23), with a typical form as a linear frequency sweep

$$H(\vec{r}, t) = H(\vec{r}) \exp \left[i \left(\omega_c t + \frac{\pi B_{\text{ch}} t^2}{T_{\text{ch}}} \right) \right], \quad -\frac{1}{2} T_{\text{ch}} \leq t \leq \frac{1}{2} T_{\text{ch}}, \quad (17)$$

where ω_c is the central frequency of the chirp, and B_{ch} and T_{ch} are the frequency bandwidth and duration, respectively, of the chirp. Because the temperature oscillation follows the laser-heating oscillation, the received pressure is also chirped, with a time lag τ dependent on the depth of the absorber. The frequency-modulated acoustic wave can be detected by a single transducer or a transducer array (24), provided that the transducer's frequency response is consistent with the chirp's bandwidth. Signal processing methods, such as frequency-domain cross-correlation or spectral analysis (21), have been employed to recover the time lag τ and the corresponding absorber's depth.

2.3. Signal-to-Noise Ratios in the Time and Frequency Domains

In both time-domain and frequency-domain PAI, the detected PA response voltage from a transducer is described by

$$V_{\text{tr}}(t) = \mathbb{F}^{-1}[\mathbb{F}(p(\vec{r}, t))Q_{\text{tr}}(\omega)\xi], \quad (18)$$

where $Q_{\text{tr}}(\omega)$ is the normalized transfer function of the transducer, and ξ is the sensitivity of the transducer at its peak frequency. A typical sensitivity range of polymer film transducers is 6–10 $\mu\text{V}/\text{Pa}$ (25, 26).

For monopole radiation, combining Equations 11, 16, and 18 gives PA response voltages in the time domain and frequency domain, respectively, as follows:

$$V_{\text{tr,TD}}(\vec{r}, t) = \frac{\xi}{4\pi v_s^2} \frac{\Gamma \eta_{\text{th}} \mu_a F_{\text{pul}}}{|\vec{r}|} \frac{d}{dt} \left[H \left(t - \frac{|\vec{r}|}{v_s} \right) \right], \quad (19)$$

$$V_{\text{tr,FD}}(\vec{r}, t) = -\frac{i\omega\beta\mu_a \bar{I}_{\text{cw}} \eta_{\text{th}} \xi}{4\pi C_p} \frac{e^{ik|\vec{r}|}}{|\vec{r}|} e^{i\omega t}, \quad (20)$$

where F_{pul} is the laser fluence in pulsed mode and \bar{I}_{cw} is the average laser fluence rate in CW mode. The ratio of peak PA response voltage in the time domain to that in the frequency domain is calculated as

$$\frac{|V_{\text{tr,TD}}|_{\text{max}}}{|V_{\text{tr,FD}}|_{\text{max}}} = \frac{F_{\text{pul}}}{\omega \bar{I}_{\text{cw}}} \frac{d}{dt} \left[H \left(t - \frac{|\vec{r}|}{v_s} \right) \right]_{\text{max}}. \quad (21)$$

If the temporal profile for pulse excitation is Gaussian—that is, $H(t) = \frac{1}{\sqrt{2\pi}} \frac{1}{\sigma} \exp(-t^2/2\sigma^2)$ —Equation 21 becomes

$$\frac{|V_{\text{tr,TD}}|_{\text{max}}}{|V_{\text{tr,FD}}|_{\text{max}}} = \frac{1}{\sqrt{2\pi e}} \frac{F_{\text{pul}}}{\omega \bar{I}_{\text{cw}}} \frac{1}{\sigma^2}. \quad (22)$$

We can estimate the ratio in Equation 22 based on the ANSI laser safety standards (27), which regulate the maximum permissible F_{pul} and \bar{I}_{cw} for pulsed and CW radiations. In the visible spectral range (400–700 nm), the maximum permissible exposures of skin to pulsed laser radiation (pulse duration of 1 ns to 0.1 μs) and to CW laser radiation (>10-s exposure time) are 20 mJ/cm^2 and

200 mW/cm², respectively. With a duration of 10 ns for pulsed excitation and a modulation frequency of 100 MHz for CW excitation, Equation 22 gives $|V_{tr,TD}|_{\max}/|V_{tr,FD}|_{\max} \sim 10^6$.

The SNR in PAI is defined as

$$\text{SNR} = \frac{\text{Maximum output peak power}}{\text{Output noise power}} = \frac{|V_{tr}(t)|_{\max}^2}{\langle V_N^2 \rangle}. \quad (23)$$

Here $\langle V_N^2 \rangle$ is normally dominated by the thermal noise, which is governed by the equation $\langle V_N^2 \rangle = 4k_B TR\Delta f$, where k_B is the Boltzmann constant, T is the absolute temperature, R is the loading resistor, and Δf is the detection bandwidth. Assuming that in the frequency domain the PA signals are detected by a phase-sensitive detector with an equivalent noise bandwidth as narrow as 1 Hz (0.125-s time constant, 12 dB/octave roll-off) and that in the time domain they are detected by a broadband detector with 100-MHz bandwidth, we have

$$\frac{\text{SNR}_{TD}}{\text{SNR}_{FD}} = \frac{|V_{tr,TD}(t)|_{\max}^2 \Delta f_{FD}}{|V_{tr,FD}(t)|_{\max}^2 \Delta f_{TD}} \sim 10^4. \quad (24)$$

Equation 24 implies that, with typical excitation and detection parameters, the SNR in the time domain is about four orders of magnitude (40 dB) higher than that in the frequency domain despite the different data acquisition times. The SNR in the frequency domain may become comparable to that in the time domain if a much longer time constant during lock-in detection is chosen. This process, however, compromises data acquisition speed. In addition, the flicker noise becomes significant when the bandwidth is less than 1 Hz, limiting the usage of extremely narrow bandwidth during lock-in detection. Despite CW lasers having a lower SNR, it is worth noting that, compared with pulsed lasers, they have the advantage of being compact and less costly, which supports the use of frequency-domain PAI in point-of-care applications (28).

3. MULTISCALE PHOTOACOUSTIC TOMOGRAPHY AND MAJOR IMPLEMENTATIONS

The primary embodiment of PAI in biomedicine is PAT. PAT can image multiscale living biological structures ranging from organelles to organs. Depending on application fields and achievable spatial resolution, PAT is divided into optical-resolution photoacoustic microscopy (OR-PAM), acoustic-resolution photoacoustic microscopy (AR-PAM), photoacoustic computed tomography (PACT), and photoacoustic endoscopy (PAE). Additionally, although ultrasonic transducers are widely used as detectors in PAT, optical-detection photoacoustic tomography (OD-PAT) has emerged as a promising alternative. In this section, we review the state-of-the-art implementations of PAT in biomedicine and summarize their advantages and limitations in **Table 1**.

3.1. Optical-Resolution Photoacoustic Microscopy

Achieving high ultrasonic resolution requires collecting high-frequency acoustic waves. However, as described in Equation 12, high-frequency acoustic waves experience strong attenuation in soft tissue. Within the optical quasi-ballistic regime—depths of less than ~ 1 mm in most biological tissue (16)—light can be focused more tightly than ultrasound. To release the dependence of resolution on acoustic frequency, OR-PAM utilizes focused light to spatially confine the excitation, resulting in an optical diffraction-limited resolution in the lateral direction (29).

Unlike X-ray imaging, OR-PAM can work in either back-reflection mode (29–33) or transmission mode (34, 35), with typical setups shown in **Figure 1a** and **b**, respectively. In both cases, the excitation laser is focused on an object to excite acoustic waves. To maximize detection sensitivity,

OR-PAM:
optical-resolution
photoacoustic
microscopy

AR-PAM:
acoustic-resolution
photoacoustic
microscopy

PACT: photoacoustic
computed tomography

PAE: photoacoustic
endoscopy

OD-PAT:
optical-detection
photoacoustic
tomography

Table 1 Comparison of various embodiments of photoacoustic tomography

	OR-PAM (29)	AR-PAM (40)	PACT (50)	PAE (54)	OD-PAT (60)
Lateral resolution	Optical	Acoustic	Acoustic	Acoustic	Acoustic
Axial resolution	Acoustic	Acoustic	Acoustic	Acoustic	Acoustic
Imaging depth in biological tissue	Optical ballistic or quasi-ballistic regime (~ 1 mm)	Optical diffusive regime (< 3 mm)	Optical diffusive regime (< 70 mm)	Optical diffusive regime (< 7 mm)	Optical diffusive regime (< 10 mm)
Data acquisition mode	Raster scan	Raster scan	Parallel	Circumferential sector scan	Parallel/raster scan

Abbreviations: AR-PAM, acoustic-resolution photoacoustic microscopy; OD-PAT, optical-detection photoacoustic tomography; OR-PAM, optical-resolution photoacoustic microscopy; PACT, photoacoustic computed tomography; PAE, photoacoustic endoscopy.

a focused ultrasonic transducer is adopted and aligned confocally with the optical lens. The lateral resolution of OR-PAM is optically determined by the laser wavelength in vacuo and the numerical aperture (NA) of the lens:

$$R_{\text{lat}} = 0.5\lambda/\text{NA}. \quad (25)$$

The axial resolution of OR-PAM is still acoustically determined by the bandwidth B of an ultrasonic transducer (36):

$$R_{\text{axi}} = 0.88v_s/B. \quad (26)$$

Ultimately, the choice of the acoustic bandwidth is based on the desired imaging depths.

To achieve volumetric imaging, the object is normally raster scanned in the transverse plane. The depth information is encoded into the time of flight of the PA wave and can be recovered by $d = v_s t$. Here, v_s is the speed of sound in the media, and t is the arrival time of the PA wave at the ultrasonic transducer. As one laser pulse must be fired at each scanning position, the imaging speed of OR-PAM is limited by the laser repetition rate. When a high-repetition-rate (e.g., 100-kHz) laser and a water-immersible microelectromechanical systems (MEMS) scanning mirror were used, a B-scan rate of up to 400 Hz over a 3-mm scanning range was reported (32).

OR-PAM works within the optical ballistic or quasi-ballistic regime (see Sidebar, Optical Ballistic, Quasi-Ballistic, and Diffusive Regimes). Owing to light scattering, the imaging depth of OR-PAM is limited to around one transport mean free path (~ 1 mm) in biological tissue (16). Beyond this depth, the lateral resolution is degraded quickly and becomes acoustically limited

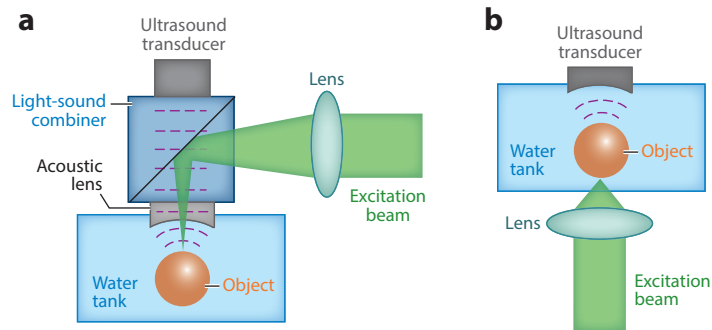


Figure 1

Optical setups of optical-resolution photoacoustic microscopy (OR-PAM) working in (a) back-reflection mode and (b) transmission mode.

OPTICAL BALLISTIC, QUASI-BALLISTIC, AND DIFFUSIVE REGIMES

Optical ballistic regime refers to depths in scattering media within which photons have undergone negligible scattering. Quasi-ballistic refers to regime depths within which photons have sustained a few scattering events but retain a strong memory of the original incidence direction. Diffusive regime refers to depths within which photons have sustained a sufficient number of scattering events and have lost nearly all memory of the original incidence direction.

(37). Compared with conventional optical microscopy technologies, OR-PAM has an advantage in providing high contrasts for endogenous chromophores without staining, enabling label-free imaging of biological tissue or cells *in vivo*. Representative images in **Figure 2** show the imaging capability of OR-PAM at different scales: vasculature structure in a nude mouse ear (**Figure 2a**), melanin in melanoma cells (**Figure 2b**), and cell nuclei (**Figure 2c**).

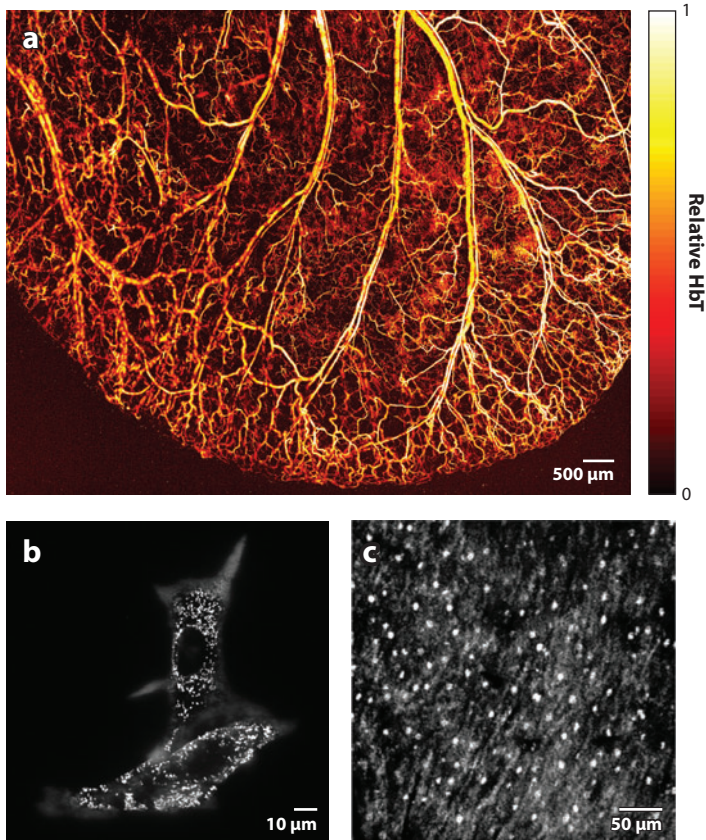


Figure 2

Photoacoustic maximum amplitude projection (MAP) images of (a) vasculature structure in a mouse ear, (b) melanin in melanoma cells, and (c) cell nuclei. Abbreviation: HbT, hemoglobin concentration. (Figure reprinted with permission from 30, 34, and 38.)

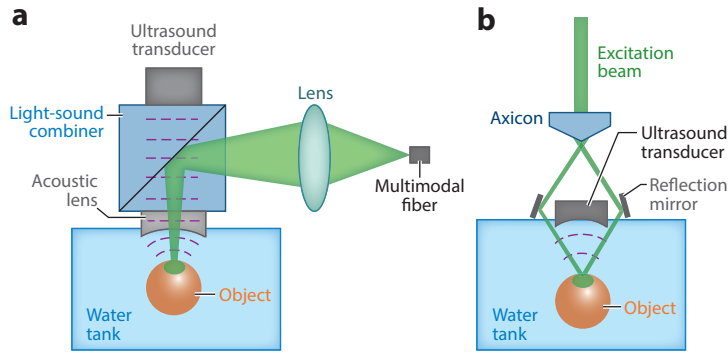


Figure 3

Optical setups of acoustic-resolution photoacoustic microscopy (AR-PAM) under (a) bright-field and (b) dark-field illumination. Note the light diffusion inside the objects.

3.2. Acoustic-Resolution Photoacoustic Microscopy

In AR-PAM, rather than light being focused on an optically diffraction-limited spot, a relatively large area is illuminated. As a result, more laser energy is allowed by the ANSI laser safety standards (27) in AR-PAM than in OR-PAM, boosting the chance of photons reaching a much greater depth.

The illumination in AR-PAM can be either bright- (**Figure 3a**; 39) or dark-field (**Figure 3b**; 40). Although the bright-field approach can deliver higher fluence to a targeted volume (39), the dark-field method has an edge in reducing surface interference to deeper PA signals (41). The spatial resolution of AR-PAM is acoustically limited along all axes. For a focused ultrasonic transducer with an aperture of diameter D and focal length l , the lateral resolution is computed as

$$R_{\text{lat}} = 0.71\lambda_0 \frac{l}{D/2}, \quad (27)$$

where λ_0 is the acoustic wavelength. The axial resolution can still be calculated by the same equation (Equation 26) as in OR-PAM (42); the only difference in the prefactor between Equation 27 and Equation 25 is that optical illumination is intensity based and acoustic detection is amplitude based. The ratio of the two prefactors is approximately the square root of 2.

In contrast to OR-PAM, AR-PAM can work in an optical diffusive regime. The achievable imaging depth is highly scalable with image resolution and depends on the central frequency and bandwidth of an ultrasonic transducer. For example, a 44- μm lateral resolution was measured at a depth of 4.8 mm with a 50-MHz ultrasonic transducer (39), and a lateral resolution of 560 μm was reported at a depth of 38 mm using a 5-MHz ultrasonic transducer (43).

3.3. Photoacoustic Computed Tomography

Rather than relying on raster scanning as in photoacoustic microscopy (PAM), PACT uses an array of ultrasonic transducers to detect PA waves emitted from an object at multiple view angles simultaneously, allowing a much faster cross-sectional or volumetric imaging speed at the expense of system and computational costs (44–46).

To accurately render an object's boundaries in two-dimensional (2D) PACT, a detector array must cover at least a π -arc directional view (44). Ultrasonic transducer arrays with various populating patterns, such as line (47), half ring (48, 49), full ring (50, 51), and hemisphere (52), have been employed and demonstrated in both animal and clinical applications.

PAM: photoacoustic microscopy

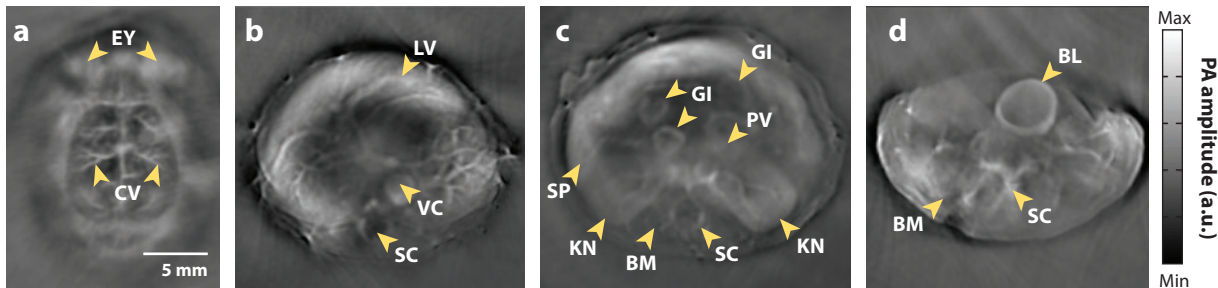


Figure 4

Photoacoustic computed tomography (PACT) images of athymic mice acquired noninvasively at various anatomical locations: (a) the brain, (b) the liver, (c) the kidneys, and (d) the bladder. Abbreviations: PA, photoacoustic; BL, bladder; BM, backbone muscle; CV, cortical vessels; EY, eyes; GI, GI tract; KN, kidney; LV, liver; PV, portal vein; SC, spinal cord; SP, spleen; VC, vena cava. (Figure reprinted with permission from 51.)

The imaging speed of PACT is normally limited by the data acquisition system. A current state-of-the-art PACT system can achieve a rate of up to 8 frames/s with a lateral resolution of $<200\ \mu\text{m}$ over a 2-cm disk-shaped region (50). **Figure 4** shows a variety of mouse organs measured by a PACT system equipped with a full-ring transducer array of 512 elements (51).

3.4. Photoacoustic Endoscopy

PAT of internal organs through endoscopy is referred to as PAE (53). Compared with routinely used clinical ultrasound endoscopy, PAE offers the same strength in spatial resolution while providing additional functional information at physiological sites.

PAE features miniaturized optical illumination and acoustic detection components that are assembled in a compact package. **Figure 5** shows a typical setup of a PAE probe, which has an outside diameter of 3.8 mm. This probe integrates ultrasonography with PAE and is designed for gastrointestinal tract imaging (54). Circumferential sector scanning is accomplished by rotating a scanning mirror, which reflects both ultrasonic waves and illumination laser pulses to a physiological site. The ultrasonic wave and pulsed laser are fired sequentially, and the ensuing ultrasound echoes and PA signals are collected by the same ultrasonic transducer after being reflected by the mirror. By using this PAE probe, researchers achieved an angular field of view of 270° and a depth of more than 5 mm in a rabbit-esophagus imaging experiment (54).

3.5. Optical-Detection Photoacoustic Tomography

Instead of being detected by piezoelectricity as in conventional ultrasonic transducers, the PA signals can also be detected by optical approaches in OD-PAT. There are two strategies: One probes PA-induced refractive index changes of the medium (55–59), and the other senses the deformation of the pressure sensor (60–62).

To measure PA-induced refractive index changes, phase imaging techniques, such as Mach–Zehnder interferometry (55) or phase contrast microscopy (59), have been exploited, with typical setups shown in **Figure 6a** and **b**, respectively. In a Mach–Zehnder-interferometry-based setup (**Figure 6a**), the sample is close to one arm of the interferometer. The acoustic waves change the refractive index of the medium along this arm (sample arm) while leaving the other arm (reference arm) unaffected. A phase difference is thus introduced between the beams from these two arms

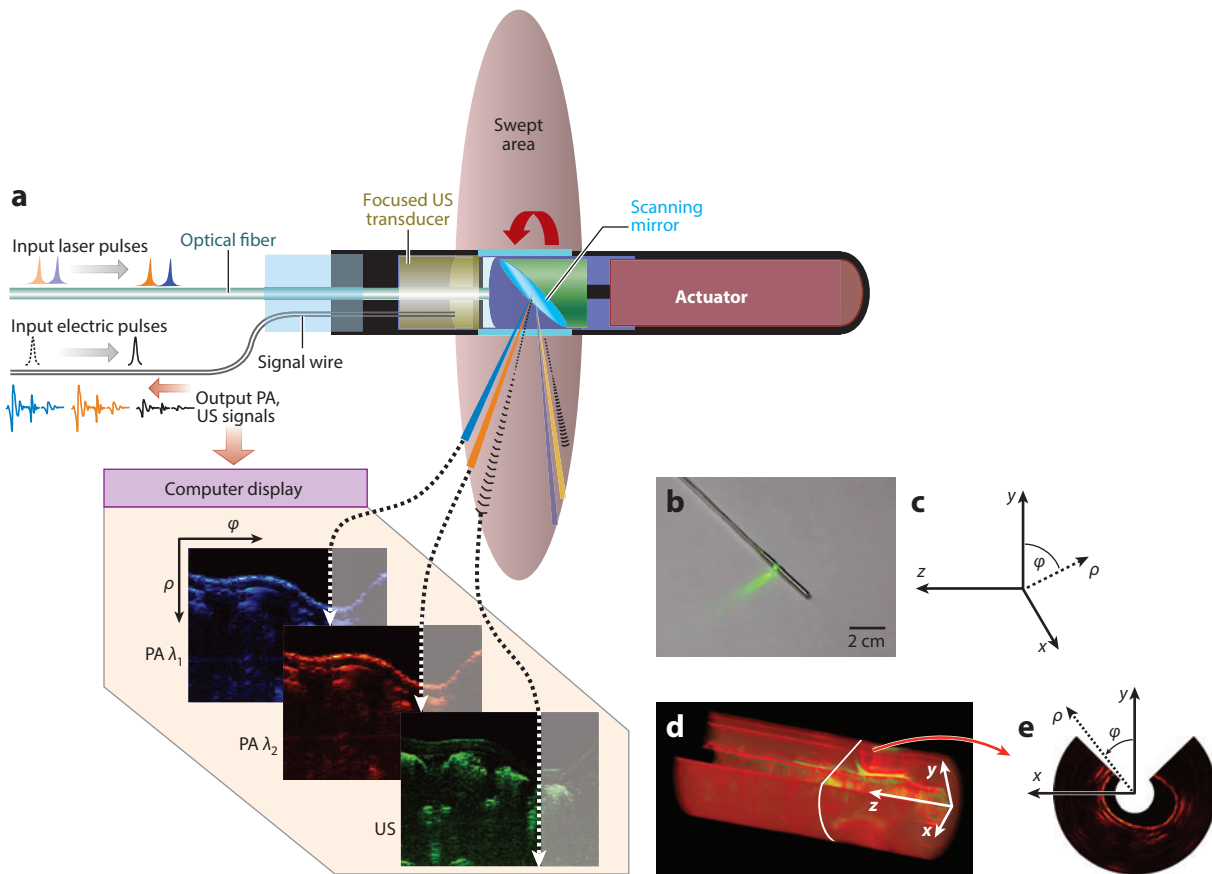


Figure 5

Simultaneous, multiwavelength photoacoustic (PA) and ultrasonic endoscopy (PAE). (a) The endoscope carries out circumferential sector scanning by rotating a scanning mirror, reflecting both ultrasonic (US) waves and laser pulses. At each angular step of the mirror ($\sim 1.42^\circ$), both the first (wavelength λ_1) and second (wavelength λ_2) pulsed laser beams are independently fired through an optical fiber; an ultrasonic transducer generates the acoustic pulse, and the same transducer then detects the ensuing PA and ultrasonic echo waves. (b) Photograph of a PAE probe. (c) Definition of Cartesian and cylindrical coordinate systems. (d) A volumetric image comprising consecutive B-scan slices. (e) A representative cross section of the image in panel (d) along the x-y plane, which shows the 270° angular field of vision of the endoscope. (Figure adapted with permission from 54.)

and can be recovered by recording their interference. To reconstruct a 3D image, the pressure field is measured at multiple positions by rotating and translating the sample.

In a phase-contrast-microscopy-based setup (Figure 6b), upon PA excitation, the local medium's refractive index change splits the probe light into perturbed (dashed red lines) and unperturbed (solid red color) beams. A $\pi/2$ phase difference is added to the perturbed beam by a phase plate located at the Fourier plane of the sample. The two light beams are then combined to produce an interference fringe on a charge-coupled device (CCD) camera. A full 2D pressure field is recovered by the phase unwrapping of the interferogram. Owing to its 2D parallel acquisition, phase contrast microscopy is superior to Mach-Zehnder interferometry in terms of imaging speed for OD-PAT (59).

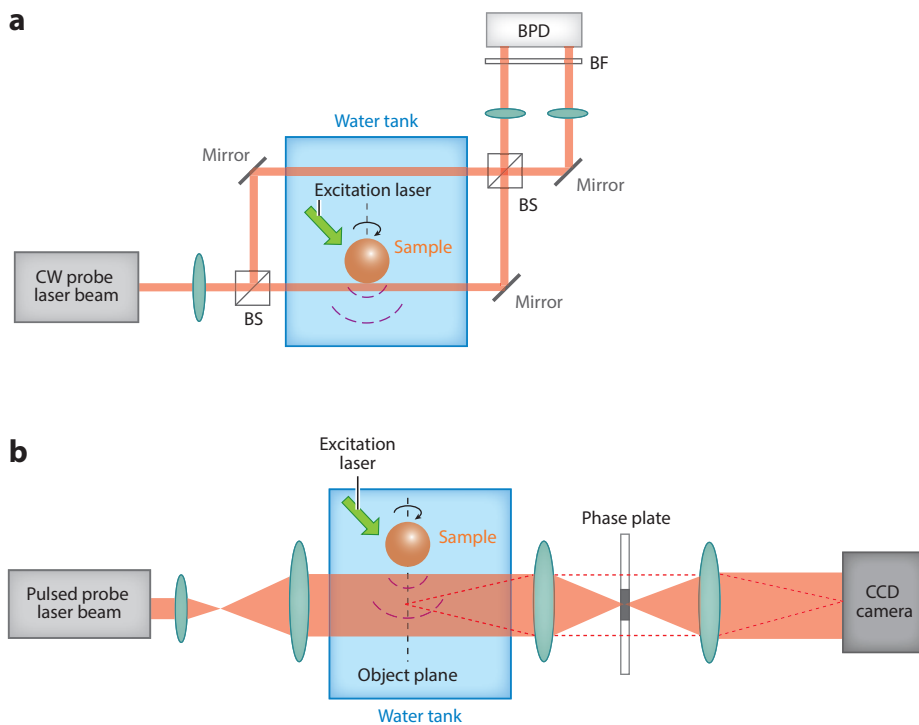


Figure 6

Optical setups of optical-detection photoacoustic tomography (OD-PAT) using (a) Mach-Zehnder interferometry and (b) phase contrast detection. Abbreviations: BF, band-pass filter; BPD, balanced photodetector; BS, beam splitter; CCD, charge-coupled device; CW, continuous wave.

The problem of measuring PA signals through sensing refractive index changes resides in the low piezooptical conversion ratio (e.g., $\partial n/\partial p = 1.47 \times 10^{-10} \text{ Pa}^{-1}$ for water) (63). State-of-the-art phase imaging techniques can recover an optical path length (OPL) change as small as 0.5 nm (64). A PA wave with a bandwidth of 20 MHz has an envelope L that spans $\sim 66 \mu\text{m}$ in space. If we treat L as the interaction distance between the pressure field and coupling water, the minimum measurable refractive index change in water can be approximated as $\Delta n = \text{OPL}/L = 7.6 \times 10^{-6}$, which corresponds to a pressure amplitude of $\Delta p = \Delta n \times \partial p/\partial n = 5.2 \times 10^4 \text{ Pa}$. The noise-equivalent pressure (NEP) of this detection scheme thus equals $12 \text{ Pa}/\sqrt{\text{Hz}}$ (20-MHz bandwidth), which is four orders of magnitude higher than the typical NEP of a broadband piezoelectric transducer ($\sim 2 \times 10^{-4} \text{ Pa}/\sqrt{\text{Hz}}$, Ferroperm, Denmark) (see Sidebar, Noise-Equivalent Pressure).

To improve the detection sensitivity, the second strategy directly measures the deformation of pressure-sensitive materials using optical resonance. Two successful implementations are

NOISE-EQUIVALENT PRESSURE

Noise-equivalent pressure (NEP) is a measure of the sensitivity of an acoustic detector. It is defined as the pressure that gives a signal-to-noise ratio (SNR) of unity in a 1-Hz output bandwidth.

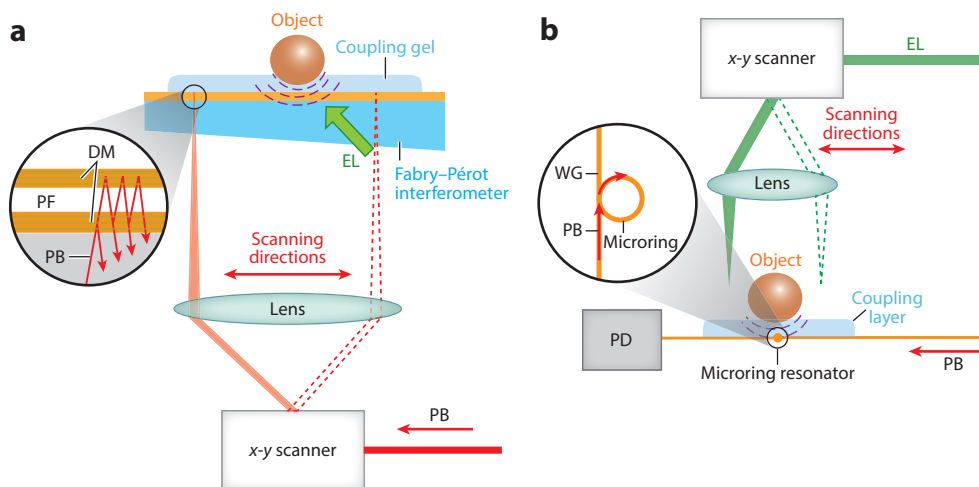


Figure 7

Optical setups of optical-detection photoacoustic tomography (OD-PAT) with (a) a high-Q polymer microring resonator and (b) a Fabry-Pérot polymer film as the pressure sensor. Abbreviations: DM, dichroic mirror; EL, excitation laser; PB, probe beam; PD, photodiode; PF, polymer film; WG, wave guide.

high-Q polymer microring resonators (**Figure 7a**) (65, 66) and Fabry-Pérot interferometers (FPIs) (**Figure 7b**) (60–62). When PA waves impinge on a pressure sensor, the pressure modulates the resonance wavelength and, thereby, the output probe laser power. The minimum NEPs reported for microring resonator-based systems and FPIs are $2.1 \times 10^{-3} \text{ Pa}/\sqrt{\text{Hz}}$ (25-MHz bandwidth) (67) and $1.8 \times 10^{-3} \text{ Pa}/\sqrt{\text{Hz}}$ (20-MHz bandwidth) (68), respectively. Currently, the FPI stands out among OD-PAT methods owing to its superior imaging performance. Two representative images, captured by a FPI, of a mouse embryo and a colorectal tumor are shown in **Figure 8a** and **b**, respectively.

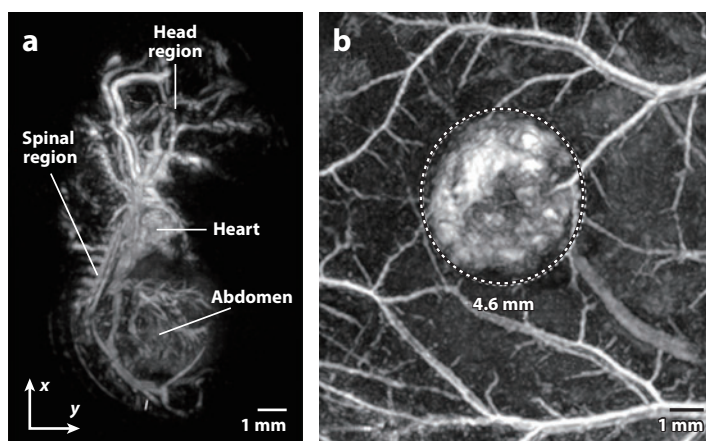


Figure 8

Photoacoustic maximum amplitude projection (MAP) images of vasculature structures in (a) a mouse embryo and (b) a colorectal tumor (LS174T) acquired by a Fabry-Pérot interferometer (FPI)-based photoacoustic computed tomography (PACT) system. (Figure reprinted with permission from 60 and 61.)

4. QUANTITATIVE PHOTOACOUSTIC SENSING AND IMAGING

4.1. Photoacoustic Oximetry

Blood oxygenation can potentially be used to measure hypermetabolism, a hallmark of cancer (69). The key measure of blood oxygenation is oxygen saturation of hemoglobin (sO_2), which is defined as the ratio of oxy-hemoglobin concentration and the total hemoglobin concentration:

$$sO_2 = \frac{C_{HbO_2}}{C_{HbO_2} + C_{HHb}}, \quad (28)$$

where C_{HbO_2} and C_{HHb} refer to the concentrations of oxy-hemoglobin and deoxy-hemoglobin, respectively. As oxy-hemoglobin and deoxy-hemoglobin have different absorption spectra $\mu_a(\lambda)$, PAT can discriminate between these two chromophores and quantify their concentrations in vivo without labeling.

As indicated in Equation 8, in time-domain PAT, the initial pressure rise after pulsed laser excitation is proportional to the product of the absorption coefficient μ_a and the local fluence F . Provided that the dependence of the fluence F on the optical wavelength λ is known, the sample's absorption spectrum $\mu_a(\lambda)$ is estimated as

$$\mu_a(\lambda) \propto p(\lambda)/F(\lambda), \quad (29)$$

where $p(\lambda)$ is the PA amplitude. After that, one can first derive the concentrations of oxy-hemoglobin and deoxy-hemoglobin by applying a spectral unmixing algorithm (70) and then calculate sO_2 distribution using Equation 28. As a representative image, **Figure 9** shows a dual-wavelength measurement by OR-PAM of sO_2 in a nude mouse ear.

The accuracy of the sO_2 relies on the SNR of each spectral channel and the condition number of the spectral component matrix (71). Although increasing the number of spectral channels and optimizing the spectral component matrix are usually restricted by available laser wavelengths, a

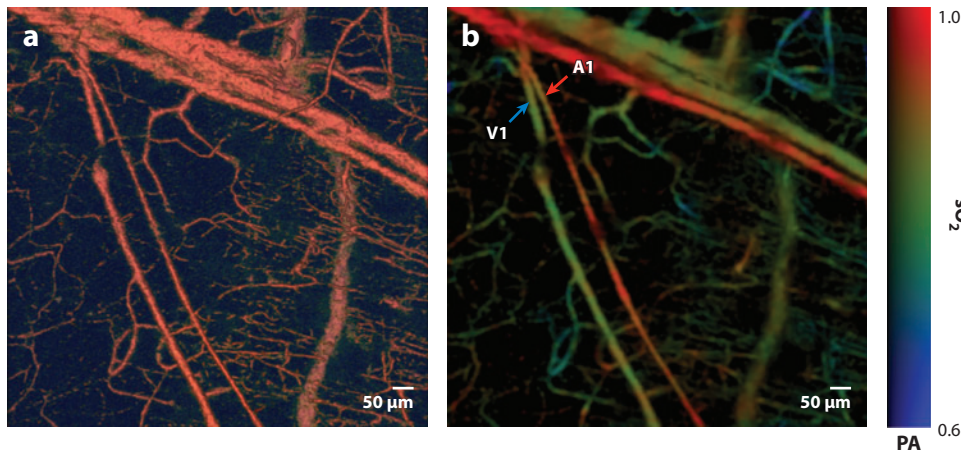


Figure 9

Structural and functional microvascular imaging by optical-resolution photoacoustic microscopy (OR-PAM) in a nude mouse ear in vivo. (a) Structural image acquired at 570 nm. (b) Vessel-by-vessel sO_2 mapping based on dual-wavelength (570 nm and 578 nm) measurements. The calculated sO_2 values are shown in the color bar. Abbreviations: A1, a representative arteriole; PA, photoacoustic signal; sO_2 , oxygen saturation of hemoglobin; V1, a representative venule. (Figure reprinted with permission from 80.)

recent study showed that improving channel SNR is more effective and can be easily achieved by employing a spectrally coded illumination (72).

However, owing to light scattering and absorption, the fluence F in deep tissue is usually heterogeneous, and its dependency on wavelength is unknown. The correction of PA signals for fluence variations, referred to as quantitative PA sensing and imaging, has been addressed via various approaches (73–76). Additionally, fluence-independent quantities, including acoustic spectra (77, 78) and molecular lifetime (79), have been used to measure blood sO₂.

4.2. Photoacoustic Thermometry

PA thermometry refers to the method of deriving the temperature distribution within a sample by measuring PA signals. PA thermometry has been implemented at both cellular (81, 82) and tissue levels (83–85). In time-domain PAT, the initial pressure rise p_0 is proportional to the Grüneisen parameter Γ , which has a linear relationship with the temperature of the surrounding medium, as given by an empirical relation (16):

$$p_0 \propto \Gamma = A + BT, \quad (30)$$

where A and B are constants, and T is the local temperature. In a nonscattering absorbing medium, Equation 30 can be rewritten for the detected pressure amplitude as

$$p(z) \propto (A + BT(z))\mu_a F_0 e^{-\mu_a z}, \quad (31)$$

where μ_a is the absorption coefficient, F_0 is the laser fluence at the sample surface, and z is the depth. If the absorbing medium is optically thin, as is a biological cell, Equation 31 is simplified to

$$p \propto (A + BT)\mu_a F_0. \quad (32)$$

With fluence correction and system calibration, the following quantity S is recovered:

$$S = k \frac{p}{F_0} = k\mu_a BT + k\mu_a A, \quad (33)$$

where k is the system's pressure sensitivity. Rearranging Equation 33 gives

$$T = \frac{1}{k\mu_a B} S - \frac{A}{B}. \quad (34)$$

As the coefficients $1/k\mu_a B$ and A/B can be calibrated for, Equation 34 can be used to reconstruct a temperature map. **Figure 10** shows temperature images of a cell during a photothermal heating process measured by OR-PAM (81). A temperature resolution of 0.2°C was achieved with an acquisition time of 3 s/C-scan.

If the sample is optically thick, as is biological tissue, the fluence varies with the depth. In such cases, the PA amplitude cannot simply be corrected with the surface fluence F_0 . Instead, a baseline PA image at a reference temperature T_0 is required (83). Dividing the PA amplitude measured at temperature T with that measured at T_0 and rearranging the equation gives

$$T(z) = \left(\frac{A}{B} + T_0 \right) \frac{p(z)}{p(z)_{T=T_0}} - \frac{A}{B}. \quad (35)$$

Equation 35 indicates that once two PA signals are acquired, the temperature can be recovered at various depths.

It is worth noting that to image absolute temperatures, the calibration must be done in the same environment as that in real-temperature imaging. However, inserting a thermocouple into

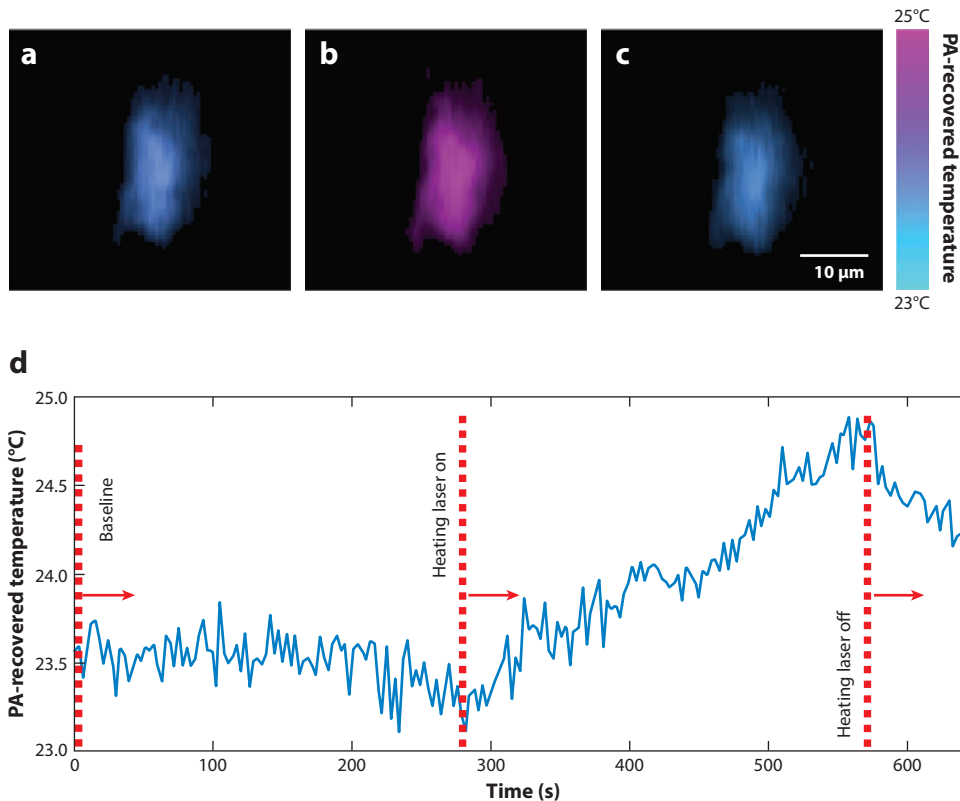


Figure 10

Single-cell temperature imaging with photothermal heating. The cell was loaded with metal particles and heated by a continuous-wave (CW) laser. Panels *a–c* show the cell temperature images before, during, and after heating, respectively. The cell is pseudocolored based on its photoacoustic (PA)-recovered temperatures. (Figure adapted with permission from 81.)

tissue is invasive and, therefore, limits PA thermometry’s use for *in vivo* studies. Calibration-free temperature imaging remains a challenge in PA thermometry.

4.3. In Vivo Photoacoustic Flowmetry

PA flowmetry refers to the method of measuring flow speed based on PA imaging. Compared with ultrasonic flowmetry (86), PA flowmetry has an advantage in low-flow-speed (<1 mm/s) measurement.

The flow velocity vector is decomposed into two components: axial speed (along the ultrasonic transducer axis) and transverse speed (perpendicular to the transducer axis). Analogous to the ultrasonic Doppler effect, the PA Doppler (PAD) effect has been observed and utilized in axial speed measurement (87, 88). The PAD shift in a clear medium is expressed as

$$f_{\text{PAD}} = f_0 \frac{v_p}{v_s} \cos \theta, \quad (36)$$

where f_0 denotes the optical modulation frequency, v_p is the flow speed of the particles, v_s is the speed of sound in the medium, and θ is the angle between the flow direction and the acoustic wave

PAD effect:
photoacoustic Doppler effect

PPAD flowmetry:
pulsed photoacoustic
Doppler flowmetry

PACS: photoacoustic
correlation
spectroscopy

propagation direction. This frequency shift equals half of that in pulse-echo Doppler ultrasound and does not depend on the direction of laser illumination.

Owing to the CW excitation, the single-frequency PAD approach cannot readily provide the depth resolution. To overcome this problem, a recent study proposed a pulsed PA Doppler (PPAD) flowmetry method (89), which measures the change in the arrival times of successive PA waves emitted by a moving cluster of absorbers by using time-domain cross-correlation. The PA waveform pairs are generated within the acoustic focus using pairs of light pulses. PPAD is analogous to the CW PAD method except that the flow speed is proportional to a fractional time shift rather than a frequency shift. Owing to the adoption of pulsed excitation, PPAD offers depth-resolved measurements with high spatial resolution.

However, when the transverse flow speed component dominates, the original PAD method fails because the transverse speed component does not contribute to the frequency shift. An alternative is based on the Doppler broadening of bandwidth, an effect due to the frequency difference between the extremities of the received acoustic wave front from an absorber moving orthogonal to the transducer axis (90). The broadening parameter B_D can be derived from the autocorrelation function of sequential A-scans, which were captured when the same type of absorbers passed through the laser focus:

$$B_D(t) \approx \frac{K}{T} \left(1 - \frac{\sum_{j=1}^n A_j(t)A_{j+1}(t)}{\sum_{j=1}^n A_j(t)A_j(t)} \right)^{1/2}, \quad (37)$$

where t is the flight time in the A-scan signal, A_j is the j th A-scan signal, T is the time interval between adjacent A-scans, n is the number of sequential A-scans used for Doppler calculation, and K is a calibration factor. A linear dependence of the broadening parameter on the flow speed was validated, and the compatibility of this method with high-resolution PAM was demonstrated in vivo (**Figure 11**). The maximum detectable flow speed was 7.4 mm/s, limited by the laser repetition rate, and the minimum detectable flow speed was 0.1 mm/s, limited by the SNR (90).

PA flowmetry is superior to other Doppler-effect-based methods, such as functional optical coherent tomography (OCT) (91) or Doppler ultrasonography (92), in blood flow measurement because PA provides unique 100% optical absorption contrast (8), whereas purely optical or ultrasonic approaches depend on optical or ultrasonic scattering, respectively. Functional OCT and Doppler ultrasonography thus suffer from a lack of sensitivity to red blood cells (RBCs), especially in measuring slow blood flow (<1 mm/s). Slowly flowing RBCs yield small Doppler shifts or bandwidth broadening, which is easily obscured by the phase noise as in OCT (93) or motion of surrounding tissue as in ultrasonography (94). In Doppler ultrasonography, to some extent one could improve sensitivity by employing high-frequency ultrasound to increase scattering at the expense of penetration. For these reasons, PA flowmetry is particularly advantageous in the measurement of low blood-flow velocities in the microvasculature (89).

For extremely slow-flow measurement, photoacoustic correlation spectroscopy (PACS) was exploited owing to its high detection sensitivity (95, 96). PACS was inspired by its optical counterpart—fluorescence correlation spectroscopy—and measures PA signal fluctuations within the laser focus volume. The autocorrelation function is defined as

$$G(\tau) = \langle \delta p(t)\delta p(t + \tau) \rangle / \langle p(t) \rangle^2, \quad (38)$$

where $\delta p(t) = p(t) - \langle p(t) \rangle$ is the fluctuation of PA signal $p(t)$, and $\langle p(t) \rangle$ denotes an ensemble average. The temporal decay profile of the autocorrelation function reveals absorbers' dwell time, which is inversely proportional to the flow speed. The measurable flow speed ranged from 14.9 $\mu\text{m/s}$ to 249 $\mu\text{m/s}$ (95).

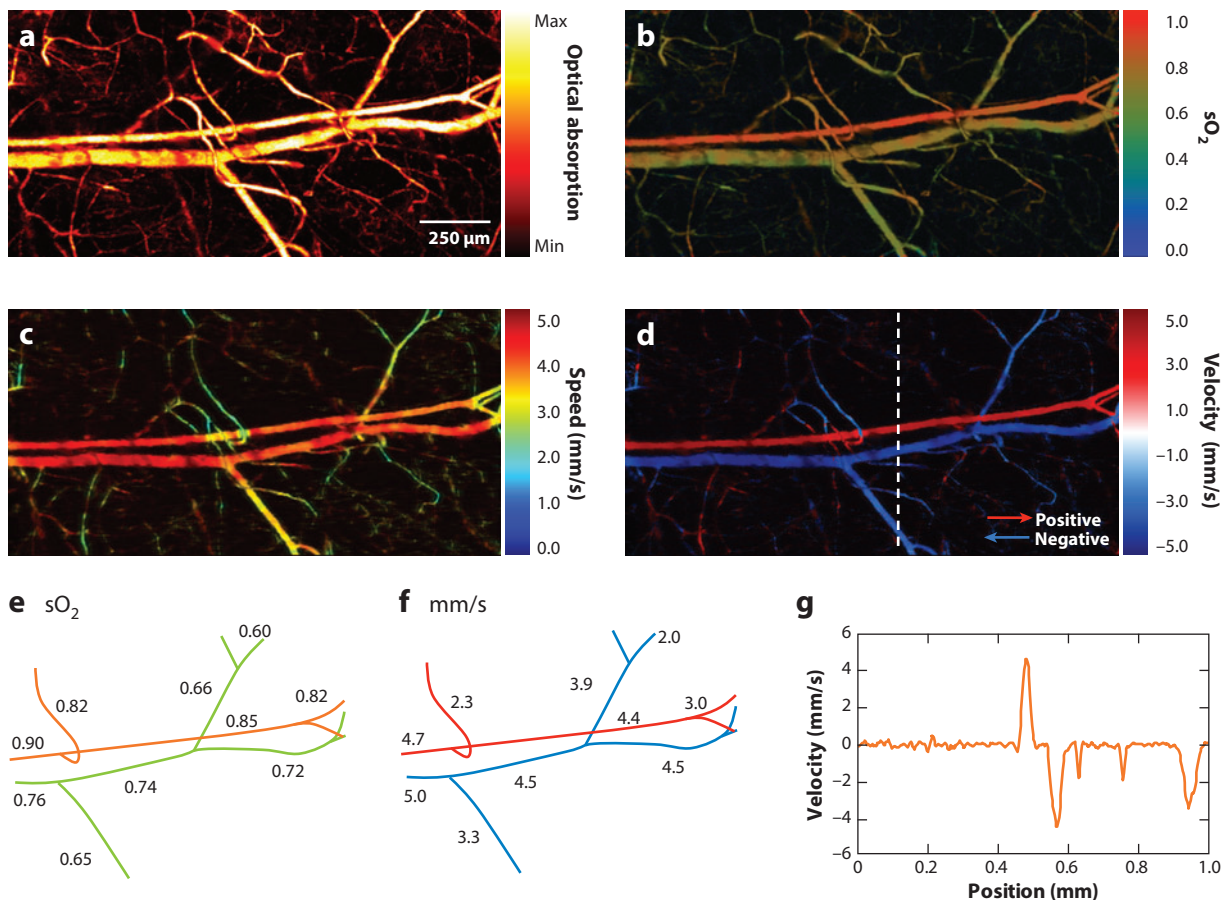


Figure 11

Photoacoustic imaging of sO₂ and blood flow in a mouse ear. Maximum amplitude projection (MAP) image of (a) a structure and (b) sO₂. MAP image of blood flow (c) speed and (d) velocity with directions. (e) Trace of sO₂ and (f) blood flow speeds along the main vascular trunk. (g) Velocity profile indicated by the dashed line in panel d. Abbreviation: sO₂, oxygen saturation of hemoglobin. (Figure adapted with permission from 90.)

4.4. In Vivo Photoacoustic Flow Cytometry

PA flow cytometry (PAFC) refers to the time-resolved detection of circulating absorbing objects (e.g., tumor cells) by means of PA sensing (97–99). Compared with conventional flow cytometry using scattering or fluorescence detection, PAFC has an advantage of not requiring extraction of cells from a living system, thereby allowing long-term study of cells in their natural biological environments.

The operation principle of in vivo PAFC is based on the excitation of selected vessels with a pulsed laser, followed by the time-resolved measurement of PA signals with an ultrasonic transducer gently held against the skin (**Figure 12**). Analogous to the laminar flow chamber in in vitro flow cytometry, here the blood or lymph vessels function as natural tubes with cell flow. As shown in **Figure 12b**, because the irradiation of blood vessels creates a constant PA background, the contrasts in PAFC can be either positive or negative. The positive contrast in PAFC can be used to detect higher absorption targets than RBCs, such as melanoma cells (100), or cells labeled with

PAFC: photoacoustic flow cytometry

nanoparticles (99), whereas the negative contrast can be used to sense lower absorption targets such as platelets or white blood cells.

A potential application of PAFC is in vivo detection of circulating tumor cells (CTCs). The spread of cancer among organs, a process known as metastasis, is the primary factor that causes cancer death. Detection of CTCs plays a critical role in evaluating metastasis as well as cancer recurrence and therapeutic efficacy (101). However, conventional in vitro diagnosis is not sensitive enough, owing to the limited volumes of blood samples. By contrast, PAFC has the capability to measure a blood volume of up to a patient's entire blood volume in vivo, resulting in a significant improvement in sensitivity (102).

The major challenge of using PAFC in detecting CTCs is being able to suppress strong PA background from blood, which can easily mask the signals from rare cell types. A recently developed imaging technique, magnetomotive PAFC, provides a solution through the magnetic accumulation and manipulation of cells targeted with magnetosensitive contrast agents (103–105). With an effective magnetic trapping system, the targeted cells were accumulated, manipulated, and then differentiated from the nonmagnetic background by motion filtering. This approach is of particular interest for clinical applications because it can sample large blood volumes in a short time while providing real-time readout.

4.5. Förster Resonance Energy Transfer Photoacoustic Microscopy

Förster resonance energy transfer (FRET) microscopy (106) is routinely used in modern biological research. However, owing to light scattering, the achievable penetration depth of FRET in biological tissue is usually less than 1 mm, limiting its application for in vivo studies. To realize deep-tissue FRET imaging, a recent study combined FRET with PAT, yielding a new imaging modality: Förster resonance energy transfer photoacoustic microscopy (FRET-PAM) (107, 108).

FRET-PAM utilizes a donor fluorophore and a nonfluorescent acceptor chromophore as a FRET pair. The emission spectrum of the donor overlaps considerably with the absorption spectrum of the acceptor, resulting in a nonradiative energy transfer when the pair are within 10 nm of each other. As the acceptor is nonfluorescent, the energy of the acceptor is released primarily via thermal dissipation, generating PA signals that are then detected by an ultrasonic transducer in the far field. Phantom results showed that PAM can be used to image FRET efficiencies through 1-cm-thick skin tissue (108).

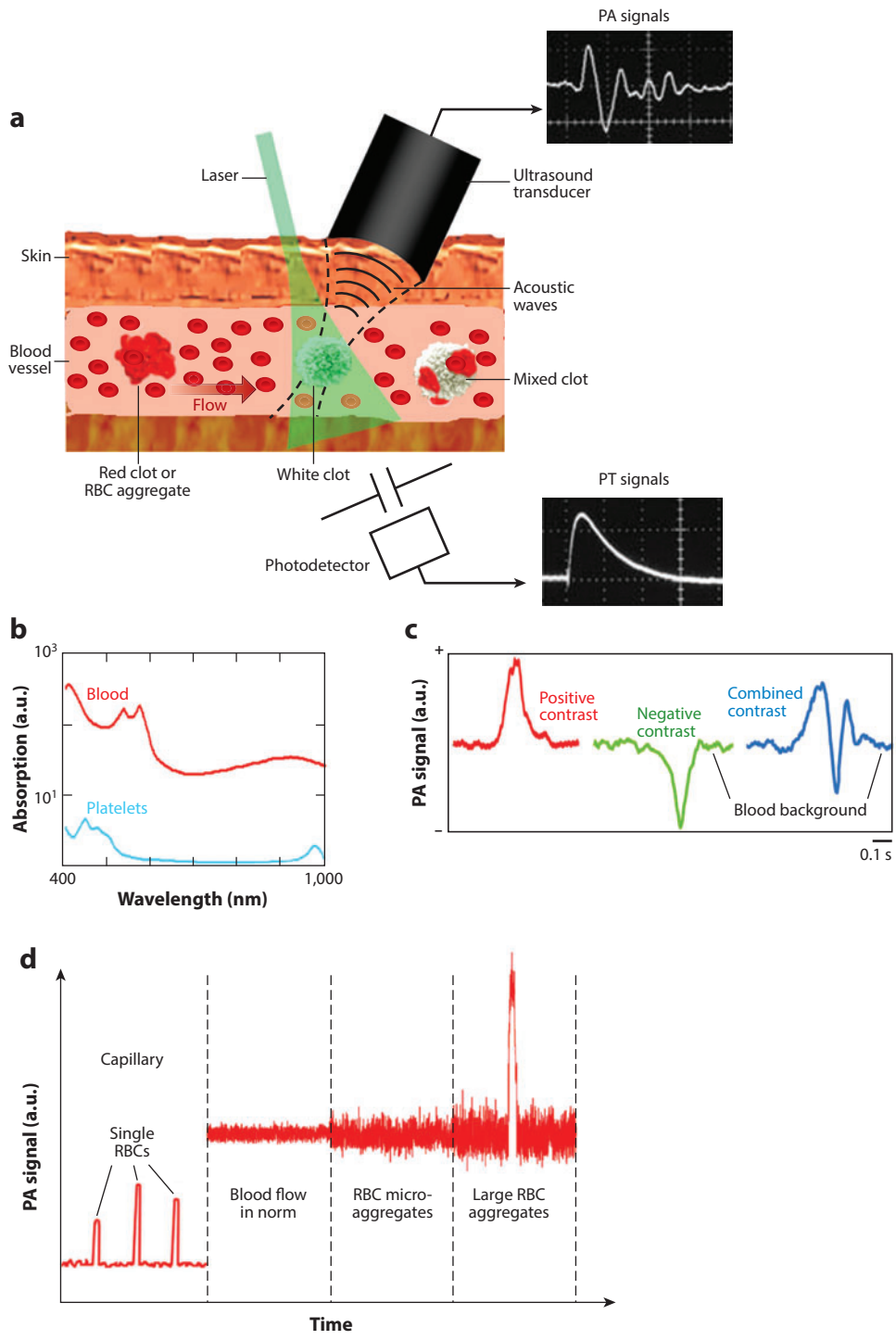
4.6. Stimulated Raman Photoacoustic Microscopy

Akin to FRET microscopy, conventional stimulated Raman (SR) microscopy also has an imaging depth limited by light diffusion (109). The recent marriage of SR with PAM offers an ideal solution to this problem (110). In SR-PAM, two excitation laser pulses (pump, ω_p , and Stokes, ω_s), separated in frequency by the vibrational frequency of a targeted molecule, excite only a specific vibrational band. The energy of this excitation state is partially transferred into heat, yielding PA signals that

→

Figure 12

Photoacoustic (PA) flow cytometry. (a) Schematic. (b) Absorption spectra of whole blood (red) and platelet-rich plasma (blue). (c) Example of PA-positive, PA-negative, and combined contrasts from circulating clots of different compositions. (d) PA signal trace dynamics obtained with PA fluctuation flow cytometry in different vessels in normal and pathological conditions leading to red blood cell (RBC) aggregation. Abbreviation: PT, photodetector. (Figure adapted with permission from 97.)



are then detected by an ultrasonic transducer. Benefitting from low acoustic scattering, an *in vivo* SR imaging experiment reported 1-mm penetration depth (111).

5. TECHNICAL ADVANCES FROM BENCH TO BEDSIDE

Translational PAT has attracted growing interest in the past decade. Its major applications are breast cancer imaging (52, 112–114), brain imaging (115), and sentinel lymph node mapping (116, 117). In this section, we review the recent technical developments in these three areas and discuss current progress toward other clinical uses.

5.1. Breast Cancer Imaging

Breast cancer is the most common cancer in women and the second leading cause of cancer death in women. Early diagnosis is crucial for the cure of breast cancer and survival of those afflicted with the disease. Conventional screening methods rely on X-ray mammography and ultrasonography; however, X-ray mammography suffers from ionizing hazard and insensitivity to tumors in dense breasts, and ultrasonography is insensitive to breast cancer at an early stage owing to low acoustic contrast.

Breast imaging is one of the first niche clinical applications of PAT owing to its great potential to overcome the limitations of X-ray mammography and ultrasonography. Three representative instruments, the LOIS-64 PAT system (112), the modified Philips iU22 system (118), and the Twente PA mammoscope (114, 119), are shown in **Figure 13a–c**, respectively. All three systems have a similar patient–instrument interface—they were built into a hospital bed and require a patient lying prone on the bed with her breast pendant through the aperture in the bed for imaging.

The LOIS-64 PAT system detects PA signals with an arc-shaped array of ultrasonic transducers (64 elements, 2.5-MHz bandwidth). The illumination with a wide laser beam orthogonal to the transducer array allows small variations of optical fluence within an area of interest, which is essential for high-quality PA imaging. The lateral resolution of the LOIS-64 system is 0.5 mm (112).

The modified Philips iU22 is the first clinical system that integrates PA, thermoacoustic, and ultrasound imaging, providing multiple, complementary contrasts for breast cancer diagnosis (118). The light delivery system and a microwave antenna are assembled into one module, allowing an easy switch operation between PA and thermoacoustic imaging. A linear ultrasonic transducer array (80 elements, 5-MHz bandwidth) is used to acquire ultrasound, PA, and thermoacoustic images. The lateral and axial resolutions of the modified Philips iU22 system are 0.72 mm and 3.5 mm, respectively.

The Twente PA mammoscope uses a flat ultrasonic transducer array (590 elements, 1-MHz bandwidth) in a parallel plate configuration. The light delivery system scans across the surface of a breast through a glass window. A mild compression is required between the glass window and the detector matrix to obtain uniform thickness of the breast and good acoustic contact with the detector. The lateral resolution ranges from 3.1 mm to 4.4 mm, and the axial resolution ranges from 3.2 mm to 3.9 mm (119).

5.2. Brain Imaging

Currently, the major imaging modalities for the human brain include X-ray computed tomography (CT), magnetic resonance imaging (MRI), and ultrasound. CT uses ionizing radiation, and MRI

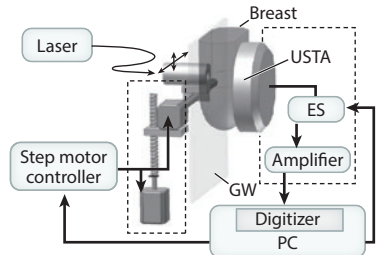
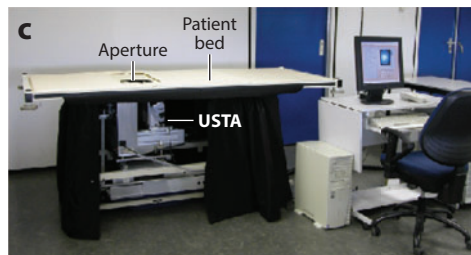
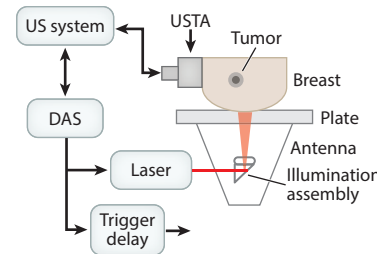
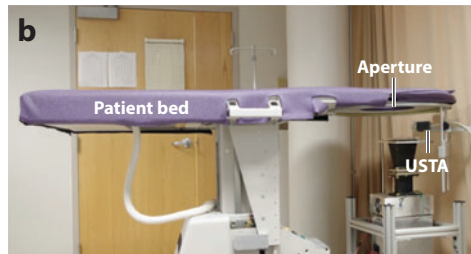
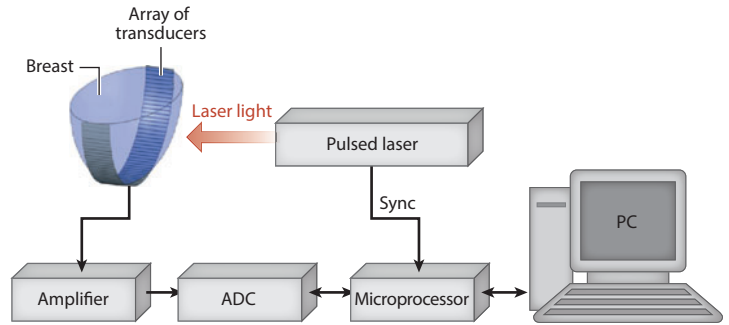
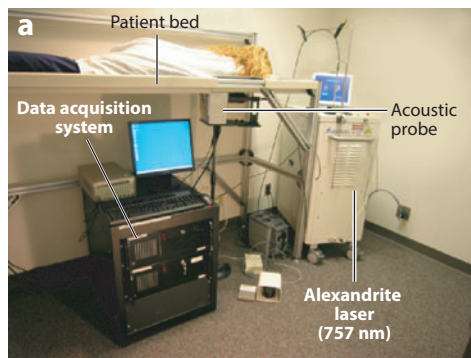


Figure 13

Clinical photoacoustic tomography (PAT) platforms for human breast imaging. (a) The LOIS-64 PAT system (112). (b) The modified Philips iU22 system (118). (c) The Twente PA mammoscope (119). Abbreviations: ADC, analog to digital converter; DAS, data acquisition system; ES, element selection; GW, glass window; US, ultrasonic; USTA, ultrasonic transducer array. (Figure adapted with permission from 112, 118, and 119.)

uses a strong magnetic field, both leading to costly setup. Ultrasonography can be used only for pediatric brains, before the closure of the fontanel. By contrast, PAT is less costly and allows superior penetration depth and functional sensitivity.

The major challenges for PAT brain imaging are the effective delivery of light through the skull and the correction for skull-induced acoustic aberrations. A skull is a highly scattering medium, attenuating both illumination light and acoustic signals. Although PAT of the brain through a skull was successfully conducted in monkeys (120, 121) and an infant (122), the feasibility of imaging through adult skulls was not demonstrated until very recently (115). As an adult skull is much thicker (~7 mm) than a monkey skull or that of an infant, the attenuation of light becomes more severe—only ~2% of photons can pass through (115). To maximize the transmitted photons,

a photon recycler was designed to reflect back the scattered photons from the surface (115). A 1-MHz spherically focused transducer that circularly scanned the skull at 200 positions achieved spatial resolution of 1 mm and an SNR of 2.4 in an ex vivo experiment (115). However, owing to the acoustic velocity mismatch and mode conversion between the skull and the coupling medium, the reconstructed PAT images were blurred. An advanced reconstruction algorithm has been developed to compensate for skull-induced acoustic aberrations and improve image fidelity with the help of adjunct CT images (123).

5.3. Sentinel Lymph Node Mapping

Sentinel lymph node (SLN) biopsy is a preferred method for axillary lymph node staging of breast cancer patients. Ultrasound guidance of minimally invasive interventions is widely performed, resulting in improved treatment outcomes and shorter recovery. However, ultrasonography cannot provide a sufficient contrast to identify the SLN, which reduces the sensitivity of ultrasound-guided fine needle aspiration biopsy (124).

To take advantage of the high sensitivity of PAT to optical absorption, a handheld array-based PAT probe was developed for SLN mapping (116, 117). The system is built upon a clinical ultrasound system (iU22, Philips Healthcare) with an integrated fiber bundle illumination, allowing handheld scanning operation as in ultrasonography. The two illumination optical beams are obliquely incident on the tissue surface as rectangles. The PA signals are detected by a linear array ultrasound probe (L8-4, Philips Healthcare) with a nominal bandwidth of 4 to 8 MHz. With this probe, the accumulation of an optical dye in the SLN, which was 2 cm below the tissue surface, was identified in a rat SLN mapping experiment (117).

5.4. Current Progress Toward Clinical Use

Breast PAT imaging is now in the clinical application phase. Using the Twente PA mammoscope, one study demonstrated that PAT images in four of six cases of patients with symptomatic breasts revealed higher-intensity regions attributed to tumor-associated vascular distributions (125). Subsequent research further investigated the clinical feasibility of PA mammography in a larger group of patients with different types of breast lesions (114). Specifically, in all 10 PAT measurements on patients, a confined region with a high contrast with respect to the background was observed, indicating the existence of malignant lesions. The investigators also discussed removal of imaging artifacts contributed by the skin surface signal and suggested that dark-field light delivery and multiview detection would probably help.

PAT for SLN mapping using methylene blue has also been tested clinically for breast cancer patients. Preliminary data demonstrated that PAT has both the required penetration depth and spatial resolution for SLN mapping (126, 127), enabling a clinician to use noninvasive diagnostic methods to stage the axilla without the morbidity risk of a surgery. As the contrast agent methylene blue has already been used in clinical SLN biopsy, a potentially expedited FDA approval for a new optical contrast agent would significantly accelerate the translation of PAT into the clinic.

Currently, PAT imaging of the human brain is still in the preclinical study phase. However, promising improvements have been achieved in the past few years, raising confidence that PAT can be a highly useful clinical tool for noninvasive functional brain imaging (115, 121, 123). **Figure 14** shows representative work that demonstrated the feasibility of PAT through an intact human adult skull (115). Main brain cortical features were observable in the PAT images and were in good agreement with the corresponding features in the photograph.

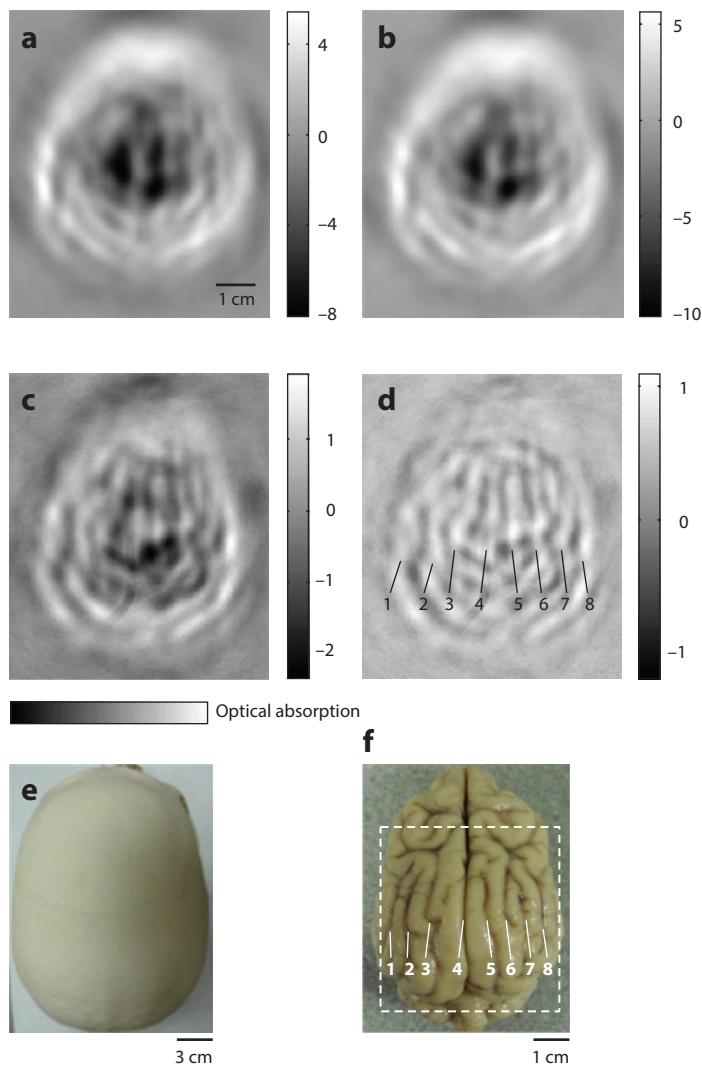


Figure 14

Photoacoustic tomography (PAT) of a canine brain through a whole adult human skull. (a) PAT image of the human skull only. (b) PAT image of a canine brain acquired through the human skull. (c) Differential image of panels *b* and *a*. (d) Image from panel *c* after high-pass filtering. (e) Photograph of the human skull from a top view. (f) Photograph of the canine brain cortex. The main brain cortical features labeled in panels *d* and *f* are in good agreement. (Figure adapted with permission from 115.)

6. CONCLUSIONS AND OUTLOOK

In summary, PAT has broad applications, from laboratory research to clinical patient care, yet additional work is still needed to further mature this technology. In this review, both fundamental principles of PAT and its state-of-the-art implementation and applications are discussed. However, an important topic that is not covered here is the development of exogenous contrast agents for biomedical PAT. A more specific article about this topic can be found elsewhere (see 128).

MRO₂: metabolic rate of oxygen—that is, the amount of oxygen consumed in a given tissue region per unit time per 100 g of tissue or of the organ of interest

Measurement of metabolic rate of oxygen (MRO₂) has emerged as a highlight of PAT. MRO₂ quantifies metabolism and thus is crucial for screening and treatment of metabolic diseases, particularly cancers and cerebral disorders. Accurate calculation of MRO₂ requires measuring three parameters: cross section of blood vessels, concentration of oxy-hemoglobin, and blood flow velocity. It is fortuitous that PAT can simultaneously measure all these independent parameters, allowing a complete assessment of MRO₂ on a single imaging modality. PAT measurement of MRO₂ in humans is expected to have a profound impact on studies of tumor metabolism and neovascularization.

Multimodality imaging integrating PAT with other complementary imaging techniques, such as fluorescence, ultrasound, and OCT, will shed new light on questions in biomedicine. PAT is sensitive to optical absorption contrasts with a preferably low fluorescent quantum yield, and fluorescence imaging provides excellent contrasts for chromophores with a high fluorescent quantum yield. Integration of PAT with fluorescence imaging facilitates studies on, for example, the effect of drugs on both cells and their surrounding microvasculature (129). Although PAT provides high detection sensitivity to optical absorption, ultrasonography and OCT provide complementary morphologic information based on acoustic and optical scattering, respectively. Combining PAT with ultrasonography or OCT will be highly useful in clinical diagnosis (116, 130, 131). In human brain imaging, ultrasound images of the skull can potentially be employed to correct for skull-induced acoustic aberrations, thereby improving the image quality of PAT.

Noninvasive quantitative imaging will become mainstream in PAT. The physical quantity that PAT directly measures is the specific optical absorption (absorbed energy per unit volume) rather than the absorption coefficient. To accurately estimate the absorption coefficient, the laser fluence within tissue must be quantified first. Quantitative PAT employing noninvasive techniques, such as diffuse optical tomography or transport optical tomography, to estimate the fluence distribution will open up new areas of investigation for in vivo tissue imaging applications.

DISCLOSURE STATEMENT

L.V.W. has a financial interest in Microphotoacoustics, Inc., and Endra, Inc.; however, neither provided support for this work.

ACKNOWLEDGMENTS

We thank Yan Liu and Sandra Matteucci for close reading of the manuscript. This work was sponsored by the National Institutes of Health (NIH) under grants R01 EB008085, R01 EB016963, R01 CA134539, U54 CA136398, R01 CA157277, R01 CA159959, and DP1 EB016986 (NIH Director's Pioneer Award).

LITERATURE CITED

1. Bell AG. 1880. On the production and reproduction of sound by light. *Am. J. Sci.* 20:305–24
2. Wang LV. 2009. *Photoacoustic Imaging and Spectroscopy*. Boca Raton, FL: CRC. 499 pp.
3. Gusev VE, Karabutov AA. 1993. *Laser Photoacoustics*. New York: Am. Inst. Phys. 271 pp.
4. Maugh TH. 1975. Photoacoustic spectroscopy: new uses for an old technique. *Science* 188:38–9
5. Kruger RA. 1994. Photoacoustic ultrasound. *Med. Phys.* 21:127–31
6. Wang LV, Zhao X, Sun H, Ku G. 1999. Microwave-induced acoustic imaging of biological tissues. *Rev. Sci. Instrum.* 70:3744–48
7. Wang X, Pang Y, Ku G, Xie X, Stoica G, Wang LV. 2003. Noninvasive laser-induced photoacoustic tomography for structural and functional in vivo imaging of the brain. *Nat. Biotechnol.* 21:803–6

8. Wang LV. 2008. Tutorial on photoacoustic microscopy and computed tomography. *IEEE J. Sel. Top. Quant.* 14:171–79
9. Hordvik A. 1977. Measurement techniques for small absorption coefficients: recent advances. *Appl. Opt.* 16:2827–33
10. Wang LV, Hu S. 2012. Photoacoustic tomography: in vivo imaging from organelles to organs. *Science* 335:1458–62
11. Culver JP, Ntzichristos V, Holboke MJ, Yodh AG. 2001. Optimization of optode arrangements for diffuse optical tomography: a singular-value analysis. *Opt. Lett.* 26:701–3
12. Calasso IG, Craig W, Diebold GJ. 2001. Photoacoustic point source. *Phys. Rev. Lett.* 86:3550–53
13. Diebold GJ, Khan MI, Park SM. 1990. Photoacoustic signatures of particulate matter: optical production of acoustic monopole radiation. *Science* 250:101–4
14. Diebold GJ, Sun T, Khan MI. 1991. Photoacoustic monopole radiation in one, two, and three dimensions. *Phys. Rev. Lett.* 67:3384–87
15. Roitner H, Bauer-Marschallinger J, Berer T, Burgholzer P. 2012. Experimental evaluation of time domain models for ultrasound attenuation losses in photoacoustic imaging. *J. Acoust. Soc. Am.* 131:3763–74
16. Wang LV, Wu H. 2007. *Biomedical Optics: Principles and Imaging*. Hoboken, NJ: Wiley-Intersci. 362 pp.
17. Szabo TL. 2004. *Diagnostic Ultrasound Imaging: Inside Out*. Amsterdam: Elsevier Acad. 549 pp.
18. Burgholzer P, Roitner H, Bauer-Marschallinger J, Grün H, Berer T, Paltauf G. 2011. Compensation of ultrasound attenuation in photoacoustic imaging. In *Acoustic Waves: From Microdevices to Helioseismology*, ed. MG Beghi, pp. 191–212. Rijeka, Croat.: InTech. 652 pp.
19. Huang C, Nie L, Schoonover RW, Wang LV, Anastasio MA. 2012. Photoacoustic computed tomography correcting for heterogeneity and attenuation. *J. Biomed. Opt.* 17:061211
20. Maslov K, Wang LV. 2008. Photoacoustic imaging of biological tissue with intensity-modulated continuous-wave laser. *J. Biomed. Opt.* 13:024006
21. Telenkov S, Mandelis A, Lashkari B, Forcht M. 2009. Frequency-domain photothermoacoustics: alternative imaging modality of biological tissues. *J. Appl. Phys.* 105:102029
22. Telenkov SA, Mandelis A. 2009. Photothermoacoustic imaging of biological tissues: maximum depth characterization comparison of time and frequency-domain measurements. *J. Biomed. Opt.* 14:044025
23. Telenkov SA, Mandelis A. 2008. Fourier-domain methodology for depth-selective photothermoacoustic imaging of tissue chromophores. *Eur. Phys. J. Spec. Top.* 153:443–48
24. Telenkov S, Alwi R, Mandelis A, Worthington A. 2011. Frequency-domain photoacoustic phased array probe for biomedical imaging applications. *Opt. Lett.* 36:4560–62
25. Karabutov AA, Savateeva EV, Podymova NB, Oraevsky AA. 2000. Backward mode detection of laser-induced wide-band ultrasonic transients with optoacoustic transducer. *J. Appl. Phys.* 87:2003–14
26. Andreev VG, Karabutov AA, Oraevsky AA. 2003. Detection of ultrawide-band ultrasound pulses in optoacoustic tomography. *IEEE Trans. Ultrason. Ferroelectr. Freq. Control* 50:1383–90
27. Laser Inst. Am. 2000. *American National Standard for Safe Use of Lasers: ANSI Z136.1–2000*. New York: Am. Natl. Stand. Inst.
28. Zhu H, Isikman SO, Mudanyali O, Greenbaum A, Ozcan A. 2013. Optical imaging techniques for point-of-care diagnostics. *Lab Chip* 13:51–67
29. Maslov K, Zhang HF, Hu S, Wang LV. 2008. Optical-resolution photoacoustic microscopy for in vivo imaging of single capillaries. *Opt. Lett.* 33:929–31
30. Hu S, Maslov K, Wang LV. 2011. Second-generation optical-resolution photoacoustic microscopy with improved sensitivity and speed. *Opt. Lett.* 36:1134–36
31. Wang L, Maslov K, Yao J, Rao B, Wang LV. 2011. Fast voice-coil scanning optical-resolution photoacoustic microscopy. *Opt. Lett.* 36:139–41
32. Yao J, Huang CH, Wang L, Yang JM, Gao L, et al. 2012. Wide-field fast-scanning photoacoustic microscopy based on a water-immersible MEMS scanning mirror. *J. Biomed. Opt.* 17:080505
33. Zhang C, Maslov K, Hu S, Chen R, Zhou Q, et al. 2012. Reflection-mode submicron-resolution in vivo photoacoustic microscopy. *J. Biomed. Opt.* 17:020501
34. Zhang C, Maslov K, Wang LV. 2010. Subwavelength-resolution label-free photoacoustic microscopy of optical absorption in vivo. *Opt. Lett.* 35:3195–97

35. Yuan Y, Yang S, Xing D. 2012. Optical-resolution photoacoustic microscopy based on two-dimensional scanning galvanometer. *Appl. Phys. Lett.* 100:023702
36. Zhang C, Maslov K, Yao J, Wang LV. 2012. In vivo photoacoustic microscopy with 7.6- μm axial resolution using a commercial 125-MHz ultrasonic transducer. *J. Biomed. Opt.* 17:116016
37. Liu Y, Zhang C, Wang LV. 2012. Effects of light scattering on optical-resolution photoacoustic microscopy. *J. Biomed. Opt.* 17:126014
38. Yao DK, Maslov K, Shung KK, Zhou Q, Wang LV. 2010. In vivo label-free photoacoustic microscopy of cell nuclei by excitation of DNA and RNA. *Opt. Lett.* 35:4139–41
39. Wang L, Maslov K, Xing W, Garcia-Uribe A, Wang LV. 2012. Video-rate functional photoacoustic microscopy at depths. *J. Biomed. Opt.* 17:106007
40. Zhang HF, Maslov K, Stoica G, Wang LV. 2006. Functional photoacoustic microscopy for high-resolution and noninvasive in vivo imaging. *Nat. Biotechnol.* 24:848–51
41. Maslov K, Stoica G, Wang LV. 2005. In vivo dark-field reflection-mode photoacoustic microscopy. *Opt. Lett.* 30:625–27
42. Hu S, Maslov K, Wang LV. 2012. Three-dimensional optical-resolution photoacoustic microscopy. In *Biomedical Optical Imaging Technologies: Design and Applications*, ed. R Liang, pp. 55–78. New York: Springer. 380 pp.
43. Song KH, Wang LV. 2007. Deep reflection-mode photoacoustic imaging of biological tissue. *J. Biomed. Opt.* 12:060503
44. Xu Y, Wang LV, Ambartsoumian G, Kuchment P. 2004. Reconstructions in limited-view thermoacoustic tomography. *Med. Phys.* 31:724–33
45. Xu M, Wang LV. 2006. Photoacoustic imaging in biomedicine. *Rev. Sci. Instrum.* 77:041101
46. Xu M, Wang LV. 2005. Universal back-projection algorithm for photoacoustic computed tomography. *Phys. Rev. E* 71:016706
47. Song L, Maslov K, Bitton R, Shung KK, Wang LV. 2008. Fast 3-D dark-field reflection-mode photoacoustic microscopy in vivo with a 30-MHz ultrasound linear array. *J. Biomed. Opt.* 13:054028
48. Buehler A, Herzog E, Razansky D, Ntziachristos V. 2010. Video rate optoacoustic tomography of mouse kidney perfusion. *Opt. Lett.* 35:2475–77
49. Razansky D, Buehler A, Ntziachristos V. 2011. Volumetric real-time multispectral optoacoustic tomography of biomarkers. *Nat. Protoc.* 6:1121–29
50. Gamelin J, Maurudis A, Aguirre A, Huang F, Guo P, et al. 2009. A real-time photoacoustic tomography system for small animals. *Opt. Express* 17:10489–98
51. Xia J, Chatni MR, Maslov K, Guo Z, Wang K, et al. 2012. Whole-body ring-shaped confocal photoacoustic computed tomography of small animals in vivo. *J. Biomed. Opt.* 17:050506
52. Kruger RA, Lam RB, Reinecke DR, Del Rio SP, Doyle RP. 2010. Photoacoustic angiography of the breast. *Med. Phys.* 37:6096–100
53. Yang JM, Maslov K, Yang HC, Zhou Q, Shung KK, Wang LV. 2009. Photoacoustic endoscopy. *Opt. Lett.* 34:1591–93
54. Yang JM, Favazza C, Chen R, Yao J, Cai X, et al. 2012. Simultaneous functional photoacoustic and ultrasonic endoscopy of internal organs in vivo. *Nat. Med.* 18:1297–1302
55. Paltauf G, Nuster R, Haltmeier M, Burgholzer P. 2007. Photoacoustic tomography using a Mach-Zehnder interferometer as an acoustic line detector. *Appl. Opt.* 46:3352–58
56. Nuster R, Zangerl G, Haltmeier M, Paltauf G. 2010. Full field detection in photoacoustic tomography. *Opt. Express* 18:6288–99
57. Nuster R, Gruen H, Reitingner B, Burgholzer P, Gratt S, et al. 2011. Downstream Fabry-Perot interferometer for acoustic wave monitoring in photoacoustic tomography. *Opt. Lett.* 36:981–83
58. Nuster R, Gratt S, Passler K, Meyer D, Paltauf G. 2012. Photoacoustic section imaging using an elliptical acoustic mirror and optical detection. *J. Biomed. Opt.* 17:030503
59. Nuster R, Paltauf G. 2012. Real-time photoacoustic imaging with optical ultrasound detection. *Proc. SPIE* 8223:82231K. doi:10.1117/12.910195
60. Laufer J, Johnson P, Zhang E, Treeby B, Cox B, et al. 2012. In vivo preclinical photoacoustic imaging of tumor vasculature development and therapy. *J. Biomed. Opt.* 17:056016

61. Laufer J, Norris F, Cleary J, Zhang E, Treeby B, et al. 2012. In vivo photoacoustic imaging of mouse embryos. *J. Biomed. Opt.* 17:061220
62. Zhang E, Laufer J, Beard P. 2008. Backward-mode multiwavelength photoacoustic scanner using a planar Fabry-Perot polymer film ultrasound sensor for high-resolution three-dimensional imaging of biological tissues. *Appl. Opt.* 47:561–77
63. Wang LV. 2001. Mechanisms of ultrasonic modulation of multiply scattered coherent light: an analytic model. *Phys. Rev. Lett.* 87:043903
64. Popescu G, Ikeda T, Dasari RR, Feld MS. 2006. Diffraction phase microscopy for quantifying cell structure and dynamics. *Opt. Lett.* 31:775–77
65. Xie Z, Chen SL, Ling T, Guo LJ, Carson PL, Wang X. 2011. Pure optical photoacoustic microscopy. *Opt. Express* 19:9027–34
66. Chen SL, Ling T, Guo LJ. 2011. Low-noise small-size microring ultrasonic detectors for high-resolution photoacoustic imaging. *J. Biomed. Opt.* 16:056001
67. Ling T, Chen SL, Guo LJ. 2011. High-sensitivity and wide-directivity ultrasound detection using high Q polymer microring resonators. *Appl. Phys. Lett.* 98:204103
68. Zhang EZ, Beard PC. 2011. A miniature all-optical photoacoustic imaging probe. *Proc. SPIE* 7899:78991F. doi: 10.1117/12.874883
69. Bateman RM, Sharpe MD, Ellis CG. 2003. Bench-to-bedside review: microvascular dysfunction in sepsis—hemodynamics, oxygen transport, and nitric oxide. *Crit. Care* 7:359–73
70. Zhang HF, Maslov K, Sivaramakrishnan M, Stoica G, Wang LV. 2007. Imaging of hemoglobin oxygen saturation variations in single vessels in vivo using photoacoustic microscopy. *Appl. Phys. Lett.* 90:053901
71. Gao L, Hagen N, Tkaczyk TS. 2012. Quantitative comparison between full-spectrum and filter-based imaging in hyperspectral fluorescence microscopy. *J. Microsc.* 246:113–23
72. Wang Y, Maslov K, Wang LV. 2012. Spectrally encoded photoacoustic microscopy using a digital mirror device. *J. Biomed. Opt.* 17:066020
73. Cox B, Laufer JG, Arridge SR, Beard PC. 2012. Quantitative spectroscopic photoacoustic imaging: a review. *J. Biomed. Opt.* 17:061202
74. Daoudi K, Hussain A, Hondebrink E, Steenbergen W. 2012. Correcting photoacoustic signals for fluence variations using acousto-optic modulation. *Opt. Express* 20:14117–29
75. Bauer AQ, Nothdurft RE, Erpelding TN, Wang LV, Culver JP. 2011. Quantitative photoacoustic imaging: correcting for heterogeneous light fluence distributions using diffuse optical tomography. *J. Biomed. Opt.* 16:096016
76. Li Z, Li H, Zeng Z, Xie W, Chen WR. 2012. Determination of optical absorption coefficient with focusing photoacoustic imaging. *J. Biomed. Opt.* 17:061216
77. Guo Z, Hu S, Wang LV. 2010. Calibration-free absolute quantification of optical absorption coefficients using acoustic spectra in 3D photoacoustic microscopy of biological tissue. *Opt. Lett.* 35:2067–69
78. Guo Z, Favazza C, Garcia-Urbe A, Wang LV. 2012. Quantitative photoacoustic microscopy of optical absorption coefficients from acoustic spectra in the optical diffusive regime. *J. Biomed. Opt.* 17:066011
79. Ray A, Rajian JR, Lee YE, Wang X, Kopelman R. 2012. Lifetime-based photoacoustic oxygen sensing in vivo. *J. Biomed. Opt.* 17:057004
80. Hu S, Maslov K, Wang LV. 2009. Noninvasive label-free imaging of microhemodynamics by optical-resolution photoacoustic microscopy. *Opt. Express* 17:7688–93
81. Gao L, Wang L, Li C, Liu Y, Ke H, et al. 2013. Single-cell photoacoustic thermometry. *J. Biomed. Opt.* 18:026003
82. Gao L, Zhang C, Li C, Wang LV. 2013. Intracellular temperature mapping with fluorescence-assisted photoacoustic-thermometry. *Appl. Phys. Lett.* 102:193705
83. Larina IV, Larin KV, Esenaliev RO. 2005. Real-time optoacoustic monitoring of temperature in tissues. *J. Phys. D Appl. Phys.* 38:2633–39
84. Shah J, Park S, Aglyamov S, Larson T, Ma L, et al. 2008. Photoacoustic imaging and temperature measurement for photothermal cancer therapy. *J. Biomed. Opt.* 13:034024
85. Pramanik M, Wang LV. 2009. Thermoacoustic and photoacoustic sensing of temperature. *J. Biomed. Opt.* 14:054024

86. Christopher DA, Burns PN, Armstrong J, Foster FS. 1996. A high-frequency continuous-wave Doppler ultrasound system for the detection of blood flow in the microcirculation. *Ultrasound Med. Biol.* 22:1191–203
87. Fang H, Maslov K, Wang LV. 2007. Photoacoustic Doppler effect from flowing small light-absorbing particles. *Phys. Rev. Lett.* 99:184501
88. Fang H, Maslov K, Wang LV. 2007. Photoacoustic Doppler flow measurement in optically scattering media. *Appl. Phys. Lett.* 91:264103
89. Bruncker J, Beard P. 2012. Pulsed photoacoustic Doppler flowmetry using time-domain cross-correlation: accuracy, resolution and scalability. *J. Acoust. Soc. Am.* 132:1780–91
90. Yao J, Maslov K, Shi Y, Taber L, Wang LV. 2010. In vivo photoacoustic imaging of transverse blood flow by using Doppler broadening of bandwidth. *Opt. Lett.* 35:1419–21
91. Ren H, Brecke KM, Ding Z, Zhao Y, Nelson JS, Chen Z. 2002. Imaging and quantifying transverse flow velocity with the Doppler bandwidth in a phase-resolved functional optical coherence tomography. *Opt. Lett.* 27:409–11
92. Yeung KW. 1998. Angle-insensitive flow measurement using Doppler bandwidth. *IEEE Trans. Ultrason. Ferroelectr. Freq. Control* 45:574–80
93. Bouwens A, Szlag D, Szkulmowski M, Bolmont T, Wojtkowski M, Lasser T. 2013. Quantitative lateral and axial flow imaging with optical coherence microscopy and tomography. *Opt. Express* 21:17711–29
94. Heimdal A, Torp H. 1997. Ultrasound Doppler measurements of low velocity blood flow: limitations due to clutter signals from vibrating muscles. *IEEE Trans. Ultrason. Ferroelectr. Freq. Control* 44:873–81
95. Chen SL, Ling T, Huang SW, Won Baac H, Guo LJ. 2010. Photoacoustic correlation spectroscopy and its application to low-speed flow measurement. *Opt. Lett.* 35:1200–2
96. Chen SL, Xie Z, Carson PL, Wang X, Guo LJ. 2011. In vivo flow speed measurement of capillaries by photoacoustic correlation spectroscopy. *Opt. Lett.* 36:4017–19
97. Galanzha EI, Zharov VP. 2012. Photoacoustic flow cytometry. *Methods* 57:280–96
98. Zharov VP, Galanzha EI, Shashkov EV, Kim JW, Khlebtsov NG, Tuchin VV. 2007. Photoacoustic flow cytometry: principle and application for real-time detection of circulating single nanoparticles, pathogens, and contrast dyes in vivo. *J. Biomed. Opt.* 12:051503
99. Galanzha EI, Shashkov EV, Kelly T, Kim JW, Yang L, Zharov VP. 2009. In vivo magnetic enrichment and multiplex photoacoustic detection of circulating tumour cells. *Nat. Nanotechnol.* 4:855–60
100. Galanzha EI, Shashkov EV, Spring PM, Suen JY, Zharov VP. 2009. In vivo, noninvasive, label-free detection and eradication of circulating metastatic melanoma cells using two-color photoacoustic flow cytometry with a diode laser. *Cancer Res.* 69:7926–34
101. Yu M, Stott S, Toner M, Maheswaran S, Haber DA. 2011. Circulating tumor cells: approaches to isolation and characterization. *J. Cell Biol.* 192:373–82
102. Galanzha EI, Shashkov EV, Tuchin VV, Zharov VP. 2008. In vivo multispectral, multiparameter, photoacoustic lymph flow cytometry with natural cell focusing, label-free detection and multicolor nanoparticle probes. *Cytometry A* 73:884–94
103. Xia J, Pelivanov I, Wei C, Hu X, Gao X, O'Donnell M. 2012. Suppression of background signal in magnetomotive photoacoustic imaging of magnetic microspheres mimicking targeted cells. *J. Biomed. Opt.* 17:061224
104. Wei CW, Xia J, Pelivanov I, Hu X, Gao X, O'Donnell M. 2012. Trapping and dynamic manipulation of polystyrene beads mimicking circulating tumor cells using targeted magnetic/photoacoustic contrast agents. *J. Biomed. Opt.* 17:101517
105. Wei C-w, Xia J, Pelivanov I, Jia C, Huang S-W, et al. 2013. Magnetomotive photoacoustic imaging: in vitro studies of magnetic trapping with simultaneous photoacoustic detection of rare circulating tumor cells. *J. Biophotonics* 6:513–22
106. Pietraszewska-Bogiel A, Gadella T. 2010. FRET microscopy: from principle to routine technology in cell biology. *J. Microsc.* 241:111–18
107. Wang Y, Wang LV. 2012. Förster resonance energy transfer photoacoustic microscopy. *J. Biomed. Opt.* 17:086007
108. Wang Y, Xia J, Wang LV. 2013. Deep-tissue photoacoustic tomography of Förster resonance energy transfer. *J. Biomed. Opt.* 18:101316

109. Min W, Freudiger CW, Lu S, Xie XS. 2011. Coherent nonlinear optical imaging: beyond fluorescence microscopy. *Annu. Rev. Phys. Chem.* 62:507–30
110. Yakovlev VV, Zhang HF, Noojin GD, Denton ML, Thomas RJ, Scully MO. 2010. Stimulated Raman photoacoustic imaging. *Proc. Natl. Acad. Sci. USA* 107:20335–39
111. Wang HW, Chai N, Wang P, Hu S, Dou W, et al. 2011. Label-free bond-selective imaging by listening to vibrationally excited molecules. *Phys. Rev. Lett.* 106:238106
112. Ermilov SA, Khamapirad T, Conjusteau A, Leonard MH, Lacewell R, et al. 2009. Laser optoacoustic imaging system for detection of breast cancer. *J. Biomed. Opt.* 14:024007
113. Jose J, Manohar S, Kolkman RG, Steenbergen W, Van Leeuwen TG. 2009. Imaging of tumor vasculature using Twente photoacoustic systems. *J. Biophotonics* 2:701–17
114. Heijblom M, Piras D, Xia W, Van Hespén JCG, Klaase JM, et al. 2012. Visualizing breast cancer using the Twente photoacoustic mammoscope: What do we learn from twelve new patient measurements? *Opt. Express* 20:11582–97
115. Nie L, Cai X, Maslov K, Garcia-Urbe A, Anastasio MA, Wang LV. 2012. Photoacoustic tomography through a whole adult human skull with a photon recycler. *J. Biomed. Opt.* 17:110506
116. Erpelding TN, Kim C, Pramanik M, Jankovic L, Maslov K, et al. 2010. Sentinel lymph nodes in the rat: noninvasive photoacoustic and US imaging with a clinical US system. *Radiology* 256:102–10
117. Kim C, Erpelding TN, Maslov K, Jankovic L, Akers WJ, et al. 2010. Handheld array-based photoacoustic probe for guiding needle biopsy of sentinel lymph nodes. *J. Biomed. Opt.* 15:046010
118. Ke H, Erpelding TN, Jankovic L, Liu C, Wang LV. 2012. Performance characterization of an integrated ultrasound, photoacoustic, and thermoacoustic imaging system. *J. Biomed. Opt.* 17:056010
119. Manohar S, Kharine A, Van Hespén JC, Steenbergen W, Van Leeuwen TG. 2005. The Twente Photoacoustic Mammoscope: system overview and performance. *Phys. Med. Biol.* 50:2543–57
120. Yang XM, Wang LV. 2008. Monkey brain cortex imaging by photoacoustic tomography. *J. Biomed. Opt.* 13:044009
121. Nie LM, Guo ZJ, Wang LV. 2011. Photoacoustic tomography of monkey brain using virtual point ultrasonic transducers. *J. Biomed. Opt.* 16:076005
122. Wang XD, Chamberland DL, Xi GH. 2008. Noninvasive reflection mode photoacoustic imaging through infant skull toward imaging of neonatal brains. *J. Neurosci. Methods* 168:412–21
123. Huang C, Nie L, Schoonover RW, Guo Z, Schirra CO, et al. 2012. Aberration correction for transcranial photoacoustic tomography of primates employing adjunct image data. *J. Biomed. Opt.* 17:066016
124. Koelliker SL, Chung MA, Mainiero MB, Steinhoff MM, Cady B. 2008. Axillary lymph nodes: US-guided fine-needle aspiration for initial staging of breast cancer—correlation with primary tumor size. *Radiology* 246:81–89
125. Manohar S, Vaartjes SE, Van Hespén JC, Klaase JM, Van den Engh FM, et al. 2007. Initial results of in vivo non-invasive cancer imaging in the human breast using near-infrared photoacoustics. *Opt. Express* 15:12277–85
126. Kim C, Erpelding TN, Jankovic L, Pashley MD, Wang LV. 2010. Deeply penetrating in vivo photoacoustic imaging using a clinical ultrasound array system. *Biomed. Opt. Express* 1:278–84
127. Kim C, Erpelding TN, Jankovic L, Wang LV. 2011. Performance benchmarks of an array-based handheld photoacoustic probe adapted from a clinical ultrasound system for non-invasive sentinel lymph node imaging. *Philos. Trans. R. Soc. A* 369:4644–50
128. Luke GP, Yeager D, Emelianov SY. 2012. Biomedical applications of photoacoustic imaging with exogenous contrast agents. *Ann. Biomed. Eng.* 40:422–37
129. Shao P, Shi W, Hajireza P, Zemp RJ. 2012. Integrated micro-endoscopy system for simultaneous fluorescence and optical-resolution photoacoustic imaging. *J. Biomed. Opt.* 17:076024
130. Jiao S, Jiang M, Hu J, Fawzi A, Zhou Q, et al. 2010. Photoacoustic ophthalmoscopy for in vivo retinal imaging. *Opt. Express* 18:3967–72
131. Li L, Maslov K, Ku G, Wang LV. 2009. Three-dimensional combined photoacoustic and optical coherence microscopy for in vivo microcirculation studies. *Opt. Express* 17:16450–55



Contents

Heart Regeneration with Engineered Myocardial Tissue <i>Kareen L.K. Coulombe, Vivek K. Bajpai, Stelios T. Andreadis, and Charles E. Murry</i> ...	1
Bioengineering the Ovarian Follicle Microenvironment <i>Lonnie D. Shea, Teresa K. Woodruff, and Ariella Shikanov</i>	29
Computational Modeling of Cardiac Valve Function and Intervention <i>Wei Sun, Caitlin Martin, and Thuy Pham</i>	53
Blood Substitutes <i>Andre F. Palmer and Marcos Intaglietta</i>	77
Optical Neural Interfaces <i>Melissa R. Warden, Jessica A. Cardin, and Karl Deisseroth</i>	103
From Unseen to Seen: Tackling the Global Burden of Uncorrected Refractive Errors <i>Nicholas J. Durr, Shivang R. Dave, Eduardo Lage, Susana Marcos, Frank Thorn, and Daryl Lim</i>	131
Photoacoustic Microscopy and Computed Tomography: From Bench to Bedside <i>Libong V. Wang and Liang Gao</i>	155
Effects of Biomechanical Properties of the Bone–Implant Interface on Dental Implant Stability: From In Silico Approaches to the Patient’s Mouth <i>Guillaume Haïat, Hom-Lay Wang, and John Brunski</i>	187
Sound-Producing Voice Prostheses: 150 Years of Research <i>G.J. Verkerke and S.L. Thomson</i>	215
3D Biofabrication Strategies for Tissue Engineering and Regenerative Medicine <i>Piyush Bajaj, Ryan M. Schweller, Ali Khadembosseini, Jennifer L. West, and Rashid Bashir</i>	247
Induced Pluripotent Stem Cells for Regenerative Medicine <i>Karen K. Hirschi, Song Li, and Krishnendu Roy</i>	277

Electroporation-Based Technologies for Medicine: Principles, Applications, and Challenges <i>Martin L. Yarmush, Alexander Golberg, Gregor Serša, Tadej Kotnik, and Damijan Miklavčič</i>	295
The Role of Mechanical Forces in Tumor Growth and Therapy <i>Rakesh K. Jain, John D. Martin, and Triantafyllos Stylianopoulos</i>	321
Recent Advances in Nanoparticle-Mediated siRNA Delivery <i>John-Michael Williford, Juan Wu, Yong Ren, Maani M. Archang, Kam W. Leong, and Hai-Quan Mao</i>	347
Inertial Focusing in Microfluidics <i>Joseph M. Martel and Mehmet Toner</i>	371
Electrical Stimuli in the Central Nervous System Microenvironment <i>Deanna M. Thompson, Abigail N. Koppes, John G. Hardy, and Christine E. Schmidt</i>	397
Advances in Computed Tomography Imaging Technology <i>Daniel Thomas Ginat and Rajiv Gupta</i>	431
Shaping Magnetic Fields to Direct Therapy to Ears and Eyes <i>B. Shapiro, S. Kulkarni, A. Nacev, A. Sarwar, D. Preciado, and D.A. Depireux</i>	455
Electrical Control of Epilepsy <i>David J. Mogul and Wim van Drongelen</i>	483
Mechanosensing at the Vascular Interface <i>John M. Tarbell, Scott I. Simon, and Fitz-Roy E. Curry</i>	505
Indexes	
Cumulative Index of Contributing Authors, Volumes 7–16	533
Cumulative Index of Article Titles, Volumes 7–16	537
Errata	
An online log of corrections to <i>Annual Review of Biomedical Engineering</i> articles may be found at http://bioeng.annualreviews.org/	



ANNUAL REVIEWS

It's about time. Your time. It's time well spent.

New From Annual Reviews:

Annual Review of Statistics and Its Application

Volume 1 • Online January 2014 • <http://statistics.annualreviews.org>

Editor: **Stephen E. Fienberg**, *Carnegie Mellon University*

Associate Editors: **Nancy Reid**, *University of Toronto*

Stephen M. Stigler, *University of Chicago*

The *Annual Review of Statistics and Its Application* aims to inform statisticians and quantitative methodologists, as well as all scientists and users of statistics about major methodological advances and the computational tools that allow for their implementation. It will include developments in the field of statistics, including theoretical statistical underpinnings of new methodology, as well as developments in specific application domains such as biostatistics and bioinformatics, economics, machine learning, psychology, sociology, and aspects of the physical sciences.

Complimentary online access to the first volume will be available until January 2015.

TABLE OF CONTENTS:

- *What Is Statistics?* Stephen E. Fienberg
- *A Systematic Statistical Approach to Evaluating Evidence from Observational Studies*, David Madigan, Paul E. Stang, Jesse A. Berlin, Martijn Schuemie, J. Marc Overhage, Marc A. Suchard, Bill Dumouchel, Abraham G. Hartzema, Patrick B. Ryan
- *The Role of Statistics in the Discovery of a Higgs Boson*, David A. van Dyk
- *Brain Imaging Analysis*, F. DuBois Bowman
- *Statistics and Climate*, Peter Guttorp
- *Climate Simulators and Climate Projections*, Jonathan Rougier, Michael Goldstein
- *Probabilistic Forecasting*, Tilmann Gneiting, Matthias Katzfuss
- *Bayesian Computational Tools*, Christian P. Robert
- *Bayesian Computation Via Markov Chain Monte Carlo*, Radu V. Craiu, Jeffrey S. Rosenthal
- *Build, Compute, Critique, Repeat: Data Analysis with Latent Variable Models*, David M. Blei
- *Structured Regularizers for High-Dimensional Problems: Statistical and Computational Issues*, Martin J. Wainwright
- *High-Dimensional Statistics with a View Toward Applications in Biology*, Peter Bühlmann, Markus Kalisch, Lukas Meier
- *Next-Generation Statistical Genetics: Modeling, Penalization, and Optimization in High-Dimensional Data*, Kenneth Lange, Jeanette C. Papp, Janet S. Sinsheimer, Eric M. Sobel
- *Breaking Bad: Two Decades of Life-Course Data Analysis in Criminology, Developmental Psychology, and Beyond*, Elena A. Erosheva, Ross L. Matsueda, Donatello Telesca
- *Event History Analysis*, Niels Keiding
- *Statistical Evaluation of Forensic DNA Profile Evidence*, Christopher D. Steele, David J. Balding
- *Using League Table Rankings in Public Policy Formation: Statistical Issues*, Harvey Goldstein
- *Statistical Ecology*, Ruth King
- *Estimating the Number of Species in Microbial Diversity Studies*, John Bunge, Amy Willis, Fiona Walsh
- *Dynamic Treatment Regimes*, Bibhas Chakraborty, Susan A. Murphy
- *Statistics and Related Topics in Single-Molecule Biophysics*, Hong Qian, S.C. Kou
- *Statistics and Quantitative Risk Management for Banking and Insurance*, Paul Embrechts, Marius Hofert

Access this and all other Annual Reviews journals via your institution at www.annualreviews.org.

ANNUAL REVIEWS | Connect With Our Experts

Tel: 800.523.8635 (US/CAN) | Tel: 650.493.4400 | Fax: 650.424.0910 | Email: service@annualreviews.org

